nature communications

Article

https://doi.org/10.1038/s41467-024-52961-8

# A plasmonic biosensor pre-diagnostic tool for Familial Mediterranean Fever

Received: 17 May 2023

Accepted: 24 September 2024

Published online: 02 October 2024

Check for updates

Idil Karaca Acari[1,7], Fatma Kurul[2,7], Meryem Beyza Avci[2], S. Deniz Yasar[2], Seda Nur Topkaya[3], Ceyhun Açarı[4], Erbil Ünsal[5], Balahan Makay[5], Süleyman Köytepe[6], Burhan Ateş[6], İsmet Yilmaz[6], Turgay Seçkin[6] & Arif E. Cetin[2]

Familial Mediterranean Fever (FMF) is an autosomal recessive genetic disorder, primarily observed in populations around the Mediterranean Sea, linked to *MEFV* gene mutations. These mutations disrupt inflammatory responses, increasing pyrin-protein production. Traditional diagnosis relies on clinical symptoms, family history, acute phase reactants, and excluding similar syndromes with *MEFV* testing, which is expensive and often inconclusive due to heterozygous mutations. Here, we present a biosensor platform that detects differences in pyrin-protein levels between healthy and affected individuals, offering a cost-effective alternative to genetic testing. Our platform uses gold nanoparticle-based plasmonic chips enhanced with anti-pyrin antibodies, achieving a detection limit of 0.24 ng/mL with high specificity. The system integrates an optofluidic system and visible light spectroscopy for real-time analysis, with signal stability maintained for up to six months. Our technology will enhance FMF diagnosis accuracy, enabling early treatment initiation and providing a cost-effective alternative to genetic testing, thus improving patient care.

Familial Mediterranean Fever (FMF) is a recessive genetic disease that originates in the Mediterranean region, particularly affecting people of Armenian, Arab, Turkish, and Jewish ancestry. For example, it affects approximately 1 in 200–1000 individuals in these populations. While it is highly prevalent in countries surrounding the Eastern Mediterranean basin, there has been an increasing number of cases reported worldwide in recent years[1–3]. Mediterranean Fever (*MEFV*) gene, associated with FMF, was defined in 1997[4,5]. FMF is characterized by specific symptoms such as episodes of fever, inflammation of serous membranes, and less frequently, complications like amyloidosis, joint restriction, and pericarditis, while it often causes leukocyte infiltration as well[6–11]. FMF is defined as the impairment of the body's inflammatory response due to variants in the *MEFV* gene located on the short arm of chromosome 16. To date, more than 300 variants have been identified in the *MEFV* gene, with many of them commonly found in exon 10[12,13]. The *MEFV* gene encodes the pyrin protein, also known as marenostrin or TRIM20[14–16]. Consequently, variants in the *MEFV* gene affect the function of the pyrin protein[17]. The pyrin protein consists of 781 amino acids and has a molecular weight of 86 kDa[16]. It is primarily found in neutrophils and macrophages, playing a crucial role in the apoptosis and inflammatory pathways. Mutated pyrin leads to an excessive inflammatory response with uncontrolled secretion of interleukin-1β[18–20]. Variants in the *MEFV* gene result in an abnormal increase in pyrin protein synthesis and disrupt the regulation of inflammation by pyrin protein[6]. While the genetic autoinflammatory disease is typically diagnosed in childhood, some individuals may not receive a diagnosis

[1]Department of Engineering Basic Sciences, Faculty of Engineering and Natural Sciences, Malatya Turgut Ozal University, Yesilyurt, Malatya, Turkey. [2]Izmir Biomedicine and Genome Center, Balcova, Izmir, Turkey. [3]Department of Analytical Chemistry, Faculty of Pharmacy, Izmir Katip Celebi University, Cigli, Izmir, Turkey. [4]Department of Pediatrics, Faculty of Medicine, Inonu University, Battalgazi, Malatya, Turkey. [5]Division of Pediatric Rheumatology, Faculty of Medicine, Dokuz Eylul University, Balcova, Izmir, Turkey. [6]Department of Chemistry, Faculty of Arts and Science, Inonu University, Battalgazi, Malatya, Turkey. [7]These authors contributed equally: Idil Karaca Acari, Fatma Kurul. e-mail: arifengin.cetin@ibg.edu.tr

until adulthood if their attacks are infrequent and mild, and they appear normal between attacks.

Currently, there is no specific laboratory test available that allows for a definitive diagnosis of FMF. The diagnosis of FMF relies on clinical symptoms, family history, evaluation of acute phase tests, response to treatment, exclusion of other familial periodic fever syndromes, and genetic laboratory data. Routine blood test results during acute attacks are not specific[21]. Genetic tests targeting the *MEFV* gene serve as the definitive diagnostic criterion for FMF[22]. However, these tests are time-consuming, require complex and costly preparation steps, and necessitate sophisticated infrastructure[23]. Despite the advantages of this diagnostic method in addressing an important disease, the lengthy duration of genetic analyses is a major obstacle for physicians aiming to use these analyses to promptly identify FMF and initiate timely treatment. While the initiation of colchicine treatment does not require genetic analyses and a clinical diagnosis of FMF is sufficient for treatment initiation, obtaining a definitive diagnosis is critical to prevent potential unnecessary treatment resulting from a false diagnosis[24]. FMF diagnosis is established primarily through the assessment of clinical symptoms. However, genetic screening is considered indispensable to both confirm the diagnosis and distinguish it from other akin conditions in the presence of patients exhibiting atypical or incomplete clinical presentations. For instance, there are numerous autoinflammatory diseases manifesting symptoms similar to FMF, and genetic analyses serve as a guiding tool in such cases. Considering the potential harm to vital organs such as kidneys caused by recurrent fever and serositis attacks in FMF, it is crucial for physicians to begin treatment based on specific parameters before the results of genetic tests are available. While initiating treatment based on symptoms and family history may provide a short-term solution, the ability to measure an indicative marker resulting from variants in the *MEFV* gene could add an important and reliable parameter for decision-making. This would enable physicians to start treatment prior to receiving the genetic test results. Variants in the *MEFV* gene lead to defective pyrin synthesis and impair the function of the pyrin protein. Interestingly, these variants can also result in abnormally increased pyrin protein synthesis, leading to higher expression levels within cells[4,6–8,10].

Recognizing the distinct difference in pyrin protein levels between healthy individuals and those with FMF, in this article, we introduce a plasmonic biosensor for the preliminary diagnosis of FMF. The biosensor platform effectively detects and quantifies the amount of pyrin protein in clinical blood samples using highly sensitive plasmonic substrates. The limit of detection achieved for pyrin protein is 0.24 ng/mL. As schematically illustrated in Fig. 1, by providing information regarding the pyrin protein levels in patient samples, in addition to the well-known symptoms and family history, our plasmonic biosensor enables physicians to pre-diagnose the disease, and promptly initiate necessary treatment while awaiting the results of genetic tests. Our biosensor platform was designed, calibrated, and tested using FMF- and FMF+ blood samples, demonstrating its potential as a clinical tool for the preliminary diagnosis of FMF. Figure 1 depicts the photograph and the schematic illustration of the plasmonic pre-diagnostic biosensor. The platform utilizes a disposable plasmonic chip, which consists of gold nanoparticles coated with anti-pyrin antibodies for label-free detection of pyrin protein. Our fabrication approach based on nanoparticle synthesis ensures stable plasmonic resonances, and the surface modification techniques used in the technology ensure the stability of the capturing mechanism for pyrin protein yielding robust sensing signals for up to six months. We also demonstrated that our surface chemistry approach allows for high specificity, as shown through selectivity and interference tests with other inflammatory proteins and various serum agents. The system hardware comprises a bright-field microscopy setup that is fiber-

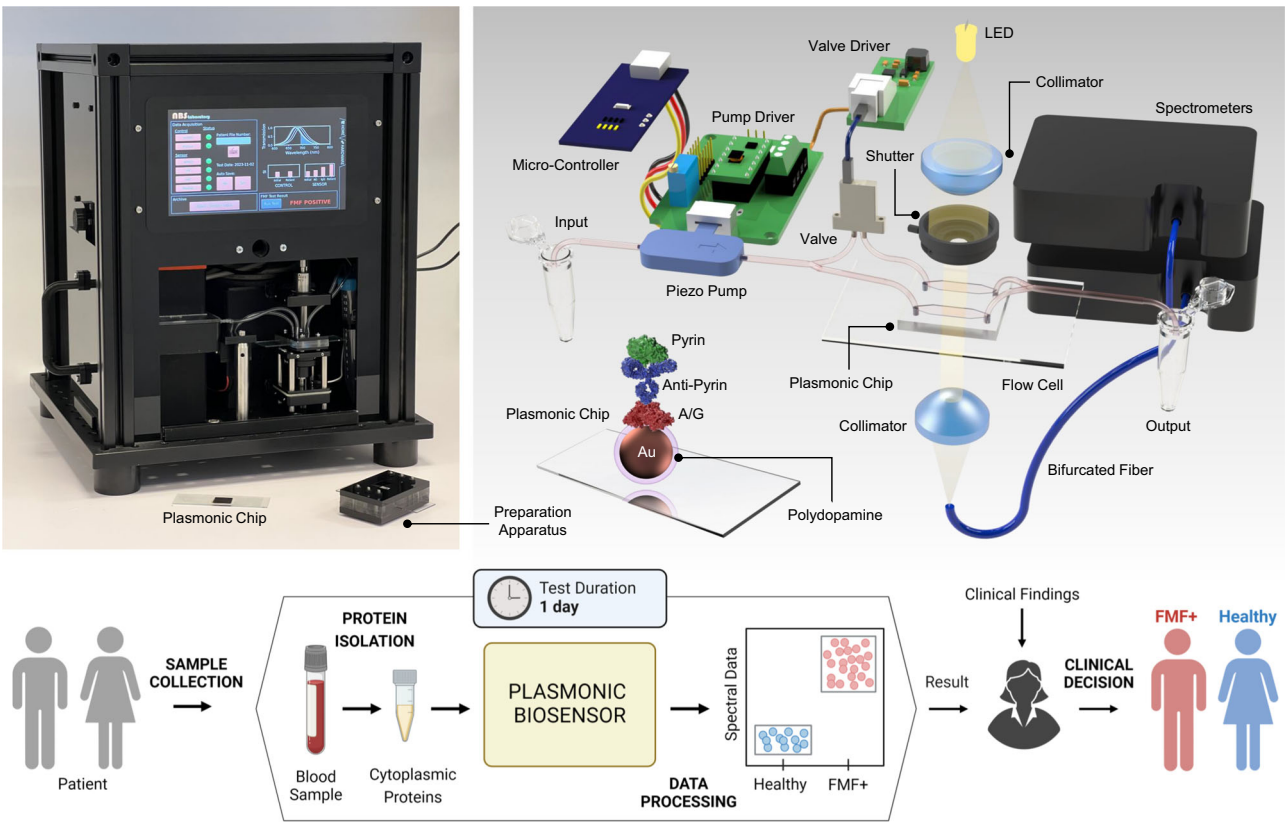


**Fig. 1 | Plasmonic biosensor platform designed for preliminary diagnosis of Familial Mediterranean Fever (FMF).** Schematic illustration shows the diagnosis of FMF based on the test results provided by the plasmonic biosensor and the clinical findings.

coupled to two spectrometers. It also includes a microfluidic setup incorporating a piezo pump, a valve, and a double-channel flow cell integrated with the plasmonic chip. The system software features a graphical user interface (GUI) that allows control of the hardware components, an algorithm for processing the raw spectral data, and a database prepared based on clinical samples that evaluates the spectral data associated with the tested samples to determine their FMF status. The biosensor platform is operated using a Raspberry Pi, eliminating the need for an external computer as it can directly provide test results to the operator. Figure SI1 in the Supplementary Information shows the flow cell within the pre-diagnostic biosensor platform, with an integrated plasmonic chip.

## Results

### System hardware

Figure 1 shows the photograph and the schematic illustration of the plasmonic biosensor used for the preliminary diagnosis of FMF. The system hardware utilizes a visible light spectroscopy setup to assess the transmission response of the nanoparticles. The plasmonic chip is illuminated by a white LED (light-emitting diode) source. Initially, the incident light is collimated using a collimator, and a shutter is employed to reduce the size of the light spot, allowing illumination of either the control or sensor location on the plasmonic chip, one at a time. The light transmitted from the plasmonic chip is collected using a fiber collimator and sent to two simultaneously operating spectrometers via a bifurcated fiber. By dividing the spectral region of interest into two 200 nm-wide spectral windows, a spectral resolution of 0.15 nm is achieved. The optical setup is assembled on an aluminum breadboard mounted on rubber dampers to minimize the effects of mechanical vibrations. The spectral measurements are based on visible light spectroscopy, and thus the spectroscopy setup is housed in a black casing to eliminate background light noise. For the targeted delivery of analytes, the platform utilizes a two-channel flow cell dedicated to control and sensor tests. Analyte delivery is ensured by a single piezo pump, with the pump outlet divided into two by using a Y-connector. A valve is integrated into the tubing connected to the control channel to prevent capturing agents such as protein A/G and IgG from reaching the nanoparticle surface in this channel. The drivers for the piezo pump and the valve are controlled by a microcontroller, enabling different flow rates by adjusting the supply voltage applied to the pump. By applying different voltages ranging from 1 V to 4.5 V at a constant frequency of 100 Hz, a linear relationship between flow rate and supply voltage is achieved. Through calibration tests conducted with PBS (a dilution solution used for all sensor tests), the flow rate range of the pump system is determined to be ~0.15 mL/min to 6.5 mL/min. The Raspberry Pi also controls the microcontroller responsible for operating the pump and the valve. The microcontroller employs pulse-width modulation (PWM) to generate an analog signal as an input for the pump driver, while the on/off voltage signals for the valve driver are applied using a relay.

### Fabrication of the plasmonic structures

For clinical applications, diagnostic test kits should ideally be disposable, requiring affordable plasmonic chips. To meet this requirement, our plasmonic chips were fabricated using a cleanroom-free method based on nanoparticle synthesis, significantly reducing the cost of the chips. Figure 2A illustrates the fabrication steps, wherein gold nanoparticles were synthesized on a glass substrate. Initially, the glass surface was cleaned with a piranha solution. Next, the glass surface was functionalized with (3-aminopropyl) triethoxysilane, which conferred an amino-functional property. Different concentrations of (3-aminopropyl) triethoxysilane, such as 5%, 10%, and 20% ethanol solutions, were studied to adjust the amount and number of functional groups on the glass surface structure. During the reaction, the glass surface was refluxed under acid catalysis and reflux temperature conditions in a sol-gel reaction. The resulting structure was characterized by washing with ethanol and ether, and its characterization measurements included FTIR (Fourier transform infrared spectroscopy), liquid contact angle, SEM (scanning electron microscope), and SEM-EDX (energy-dispersive X-ray) analyses. The number of amino groups on the surface was determined analytically using the back titration method[25]. Subsequently, nanoparticle synthesis was conducted on the surface with a sufficient number of amino groups. The citrate reduction method was employed for synthesis, where a 1 mL solution of 1% trisodium citrate was added to the oil bath, and a 50 mL solution of $HAuCl_4$ was mixed with this solution. The reaction was allowed to proceed for 30 min with high stirring. After the process, the mixture was cooled to room temperature, resulting in a gold nanoparticle solution. The size, morphology, and distribution of nanoparticles in the solution were determined using TEM (transmission electron microscopy), Zeta Sizer, and X-ray spectroscopic techniques. The gold nanoparticles with the appropriate size and morphology were then coated onto the clean glass surface using the thermal annealing method at 110 °C for two hours under a nitrogen atmosphere (under vacuum conditions). Based on measurements with a particle size analyzer, the average nanoparticle size used for synthesis was found to be ~40 nm. The nanoparticles were further coated with polydopamine using the dip-coating method, which was performed at room temperature in a 0.5 mg/mL polydopamine solution prepared with 10 mM tris buffer at pH 8.5. The dip-coating method parameters, such as dipping speed, time, retraction speed, solution concentration, and number of dips, were characterized to determine the optimal surface film. We used the polydopamine film to stabilize the nanoparticles and promote analyte attachment[26].

### Optical properties of the plasmonic chip

To ascertain the underlying physical mechanisms responsible for the plasmonic resonances supported by the gold nanoparticles, we conducted finite difference time domain (FDTD) simulations. (See the "Methods" section for the details of the numerical simulations) The optical properties of the plasmonic chip, based on gold nanoparticles, were characterized using visible light spectroscopy. These nanoparticles utilize the unique optical properties of surface electromagnetic waves, known as surface plasmons, which enable the label-free detection of biomolecular interactions[27]. In the plasmonic chip, the nanoparticles are synthesized and distributed randomly over the glass substrate, supporting a localized surface plasmon mode. This mode is excited at a specific wavelength determined by the particle size. In Fig. 2B, the optical response of the plasmonic chip is shown. For example, gold nanoparticles exhibit a plasmonic resonance at ~521 nm, with a linewidth of ~51 nm. Figure 2C illustrates the cross-sectional profile of the electric field along the direction of propagation (z-axis), demonstrating that the hot spots with large local electromagnetic fields primarily concentrate along the particle wall. Importantly, these hot spots extend extensively within the medium rather than being confined within the supporting glass substrate. This characteristic makes them highly accessible to the analytes of interest on the plasmonic sensing surface. This accessibility is crucial for label-free biosensing technologies that rely on sensing-by-binding methodologies. In such methods, light-matter interactions creating refractive index changes, are used to determine the presence of targeted analytes. Figure 2D shows the nearfield distribution at the center of a single nanoparticle (highlighted with a white dashed line in Fig. 2C) along the xy-plane. Under an unpolarized incident light source, electromagnetic fields are mainly localized around the edges in all directions.

### Preparation of the plasmonic chips

The synthesis of the gold nanoparticles was performed on a microscope glass slide. To reduce the fabrication cost, we selectively

https://doi.org/10.1038/s41467-024-52961-8

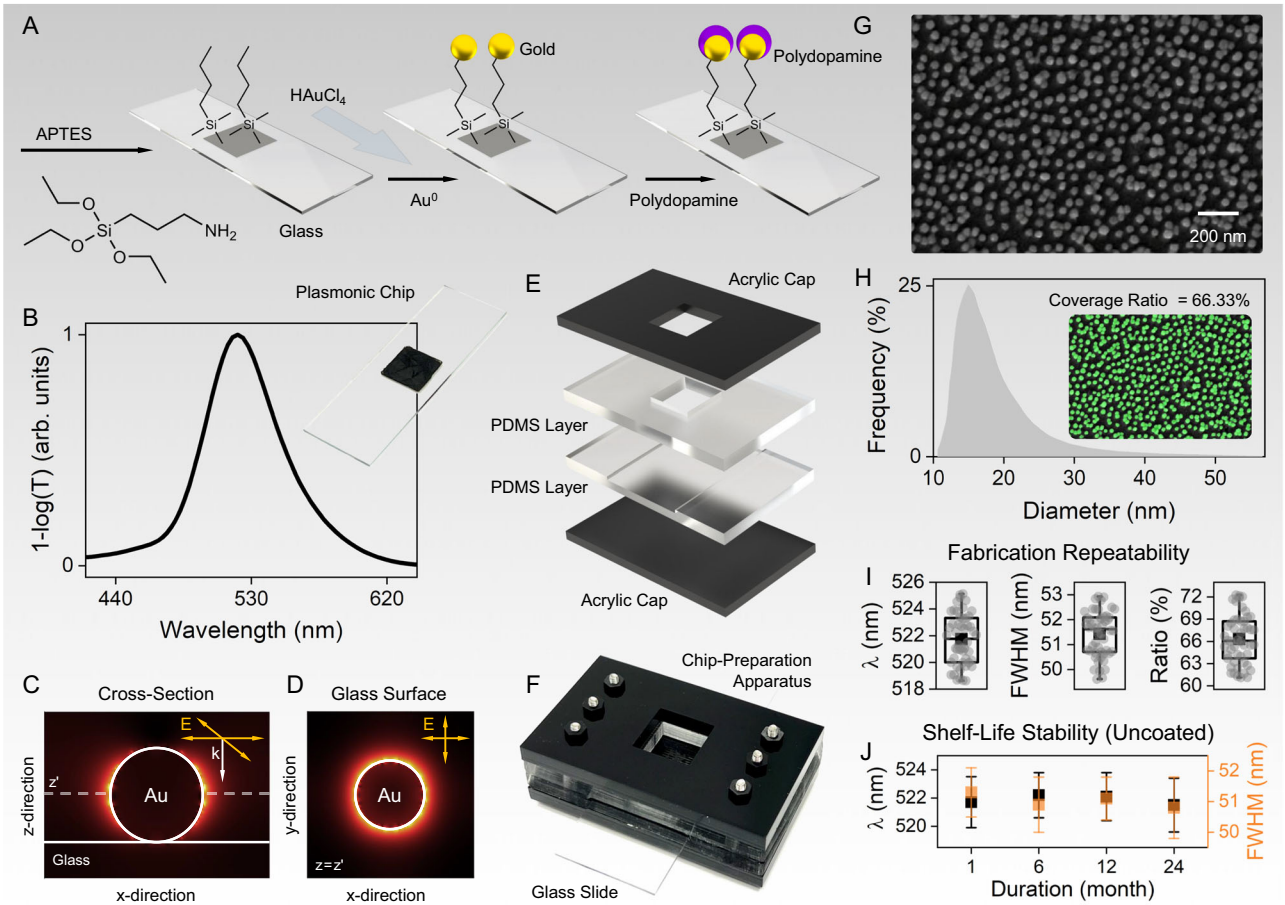


**Fig. 2 | Gold nanoparticle-based plasmonic chip utilized in the pre-diagnostic platform. A** Realization of plasmonic chips based on nanoparticle immobilization on a glass substrate using a synthesis and chemical modification method. **B** Experimentally obtained plasmonic resonance supported by the synthesized gold nanoparticles (T = Optical transmission). The inset in the figure shows the photograph of a plasmonic chip. **C** Cross-sectional electric field profile calculated at the plasmonic resonance. **D** Electric field profile calculated at z = z′ (highlighted with a white dashed line in Fig. 2C) along the xy-plane. The figure displays the propagation (**k**) and polarization (**E**) directions of the incident light source. **E** Schematic illustration of the constituent elements of the chip-preparation apparatus. **F** Photograph of the chip-preparation apparatus with a glass slide sandwiched inside. **G** SEM image of the gold nanoparticles bounded on the glass surface. **H** Zeta Sizer results demonstrating particle distributions based on diameter. Figure inset shows the substrate surface covered with gold particle (highlighted with green), demonstrating a 66.33% coverage ratio. **I** Variations within the resonance wavelength (λ, left) and the linewidth (full-width half-maximum - FWHM, middle) of the transmission resonance supported by $n = 50$ plasmonic chips with different surface coverage ratios (right). The box plot represents the interquartile ranges, and the black squares are the average values of the data. **J** Variations in the spectral position (λ, black) and the linewidth (orange) of $n = 10$ plasmonic chips over a 24-month period. In the figure, squares correspond to the mean values and the error bars represent double the standard deviation.

coated only a specific area on the plasmonic chip surface, considering the spectral measurements performed on a small area. For this purpose, we developed a chip-preparation apparatus. Figure 2E, F show the schematic illustration and photograph of the chip-preparation apparatus, respectively. The apparatus consists of two layers of polydimethylsiloxane (PDMS) and two acrylic caps, with the glass slide sandwiched between the PDMS layers. The molds used to create the PDMS layers were manufactured using resin-based 3D printing. The top PDMS layer features a square hole that defines the area for nanoparticle synthesis on the glass slide, while the bottom PDMS layer has a rectangular groove with the width of the microscope glass slide to hold the slide in position. The top acrylic cap, concentric with the hole in the top PDMS layer, is used to secure the glass slide. To ensure a leak-free setup, we tightened the PDMS layers using six screws, taking advantage of the deformability of PDMS to prevent the glass slide from breaking. Once the glass slide is positioned within the chip-preparation apparatus, we conducted the nanoparticle synthesis protocol on the designated open area of the glass slide. Figure 2B-inset shows the photograph of the fabricated plasmonic chip, with the nanoparticles synthesized on the black area.

In our pre-diagnostic technology, plasmonic chips were created by synthesizing gold nanoparticles. 3-aminopropyltriethoxy silane (APTES) served as the binding molecule to affix gold nanoparticles to the glass surface. The APTES structure forms Si–O bonds through a sol-gel reaction with the –OH groups on the substrate surface, resulting in an amino-functional surface structure. Although an alternative molecule forming a much stronger covalent bond with the Au nanoparticles, e.g., (3-mercaptopropyl)trimethoxysilane (MPTES), could have been chosen as the binding molecule, we preferred APTES for our fabrication methodology. MPTES is an organosilane with three alkoxy groups capable of reacting with hydroxyl groups on the substrate surface to form Si–O bonds, leaving terminal functional thiol groups available for immobilization. Both APTES and MPTES are commonly used for surface binding of AuNPs[28]. However, there is no quantitative evidence to determine which functionality is superior for incorporating AuNPs in the immobilization process[28]. In this context, the weak interaction is attributed to electrostatic bonding, while the strong interaction results from covalent bonding. Both bonding agents effectively bind and coat the Au groups onto the surface[28]. Despite these general considerations, four specific reasons justify the preference for APTES in our study.

(i) The interaction of the APTES structure with gold nanoparticles is weaker than the interaction of 3-mercaptopropyl groups with gold nanoparticles. This characteristic ensures that it does not disrupt the crystal structure of gold nanoparticles, maintaining their integrity[29]. Additionally, the weak interaction results in a lower degree of passivation compared to thiols, making the gold surface less passivated[30]. Consequently, subsequent modifications could be easily carried out. (ii) Amino groups on the APTES molecule, adhering to the glass surface via sol-gel chemistry, bind to gold nanoparticles through electron transfers and electrostatic interactions. In contrast, HS- groups on MPTES possess two unshared electron pairs on the S atom, leading to a stronger interaction with gold nanoparticles[31,32]. This stronger interaction could potentially result in irregular and multilayer bonding, as well as single-row gold accumulation on the surface, which is undesirable for optical sensors. (iii) In this study, our focus was on a pre-diagnostic technology employing disposable measurement units. Achieving cost-effective measurements with disposable chips necessitates a low-cost disposable sample unit, which is a requirement met with the use of APTES. (iv) As demonstrated in the literature, APTES allows for faster derivation of gold films, providing a practical advantage in the context of this study[33].

### Repeatability and stability of chip fabrication

Figure 2G shows the scanning electron microscopy (SEM) images, revealing well-distributed random gold nanoparticles on the glass surface. The results of Zeta Sizer in Fig. 2H shows the particle size distribution, demonstrating an average particle size of ~40 nm. The SEM image further shows that gold nanoparticles cover ~66% of the total surface, as indicated in Fig. 2H-inset (green areas represent the gold-covered surface). Our fabrication methodology based on nanoparticle synthesis results in random antenna formations on the dielectric surface, which could lead to batch-to-batch variations in the position and linewidth of the plasmonic resonance supported by the nanostructures. Figure 2I compares the variations in the spectral position (left) and the linewidth (middle) of the plasmonic resonance with the coverage ratio of the glass surface by the gold nanoparticles (right). Analyzing 50 plasmonic chips, we found that the surface coverage ratio centers at 66.32% with a standard deviation of 3.32%. These variations in the particle distribution lead to variations in the optical properties of the plasmonic chips, e.g., the resonance location is centered at 521.74 with a standard deviation of 1.91 nm and the linewidth is centered at 51.43 nm with a standard deviation of 0.91 nm. These small variations demonstrate the robustness and repeatability of our fabrication process. As an important note, despite the batch-to-batch variations resulting in minor variations in the optical properties of the plasmonic chips, they could be critical when evaluating diagnostic conditions based on low biomarker concentrations in bodily fluids. As explained in the next section, batch-to-batch variations were eliminated by evaluating each test using its own plasmonic chip, where the position and linewidth of the transmission resonance were solely responsible for the calculations performed with the associated plasmonic chip.

As an additional point to consider, while our technology is based on realizing the plasmonic chips through particle synthesis and offers cost-effectiveness, another crucial factor for the commercial applications of diagnostic platforms relying on sensing-by-binding methodology is the shelf-life stability of the uncoated plasmonic chips. Figure 2J depicts the average spectral position and linewidth of the plasmonic resonance for 10 plasmonic chips monitored over a 24-month period, revealing minimal variations in these two parameters, each remaining below 0.5 nm. For example, the transmission resonance has a mean spectral position of ~521.9 nm with a standard deviation of 0.33 nm, where the linewidth is ~51 nm with a standard deviation of 0.22 nm. This analysis underscores the robust shelf-life stability afforded by our fabrication method, which is an essential attribute for potential commercial applications in the field of diagnostics.

### Manufacturing process of the flow cell

For label-free applications, one traditional method of introducing biomolecules to the sensor surface is physical immobilization through pipetting, where the analytes of interest randomly bind to the surface. However, this technique limits the consistency and reproducibility of sensing data[34]. In our plasmonic pre-diagnostic platform, we adopted the targeted delivery of analytes methodology, which utilizes a flow cell comprising two microfluidic channels for control and sensor tests (Fig. 3A). The control channel is employed to generate reliable and accurate biosensing signals by eliminating noise caused by biological, optical, or mechanical fluctuations. The flow cell consists of two layers of polydimethylsiloxane (PDMS), where the top PDMS layer contains the microfluidic channels, and the bottom PDMS layer has a rectangular groove with the width of a microscope glass slide to position it. Similarly, the molds used for creating the PDMS layers were produced using resin-based 3D printing. Traditionally, PDMS-based components are bonded to the sensing surface, limiting their reusability. To address this limitation, we designed a user-friendly flow cell holder that consists of two acrylic caps, ensuring a leak-free microfluidic system without the need for PDMS bonding. As depicted in Fig. 3A, the two acrylic caps are identical and used to secure the PDMS layers. They feature two holes aligned with the control and sensor channels in the top PDMS layer, allowing light transmission. Four screws were utilized to tighten the PDMS layers, ensuring a leak-free flow cell design while preventing the glass slide from breaking.

### Limit of detection of the biosensor platform

As surface plasmons are strongly concentrated on the surface of the metallic particles, their optical properties are very sensitive to changes within the refractive index of the adjacent medium, which can alter the excitation wavelength of the surface plasmons. For example, when an analyte is captured on the metallic surface using its capturing ligand, the effective refractive index increases, thereby red-shifting the excitation wavelength of the surface plasmons. By employing a ligand with high affinity for the targeted analyte, the spectral variations in the optical response of the nanoparticles can indicate the presence of this analyte. The transmission resonance of nanoparticles coated with anti-pyrin antibody exhibits different spectral shifts depending on the amount of pyrin protein present in the FMF− and FMF+ samples. Healthy individuals have a certain amount of pyrin protein, which increases dramatically in FMF patients[35,36]. Consequently, the spectral shift within the transmission resonance is much larger for the patient samples compared to the healthy samples. Our pre-diagnostic biosensor utilizes this distinct variation in the spectral shift to determine the FMF status of clinical samples.

Figure 3A-inset shows the schematic illustration demonstrating the capturing mechanism for the pyrin protein on the gold sensing surface via its capturing antibody. (See the “Methods” section for the details of the surface modification methodology for capturing pyrin protein) In the flow cell, the biological agents in both commercial and clinical samples were diluted in PBS. Figure 3B shows the transmission response of the nanoparticles for different biological agents under a PBS solution. Here, the initial transmission resonance located at ~675.5 nm (black curve) shifted to ~677.4 nm (orange curve) and ~686.7 nm (blue curve) after the attachment of 100 μg/mL protein A/G and 100 μg/mL protein IgG, respectively. Finally, 100 μg/mL pyrin protein shifted the transmission resonance to ~693.6 nm (green curve). Here, the high concentrations of protein A/G and IgG were used to fully coat the sensing surface with antibodies, ensuring that even samples with very low amounts of pyrin protein could still be captured on the surface. As a result, the biomass on the sensing surface could vary even at very low pyrin concentrations, creating a spectral shift that provides

https://doi.org/10.1038/s41467-024-52961-8

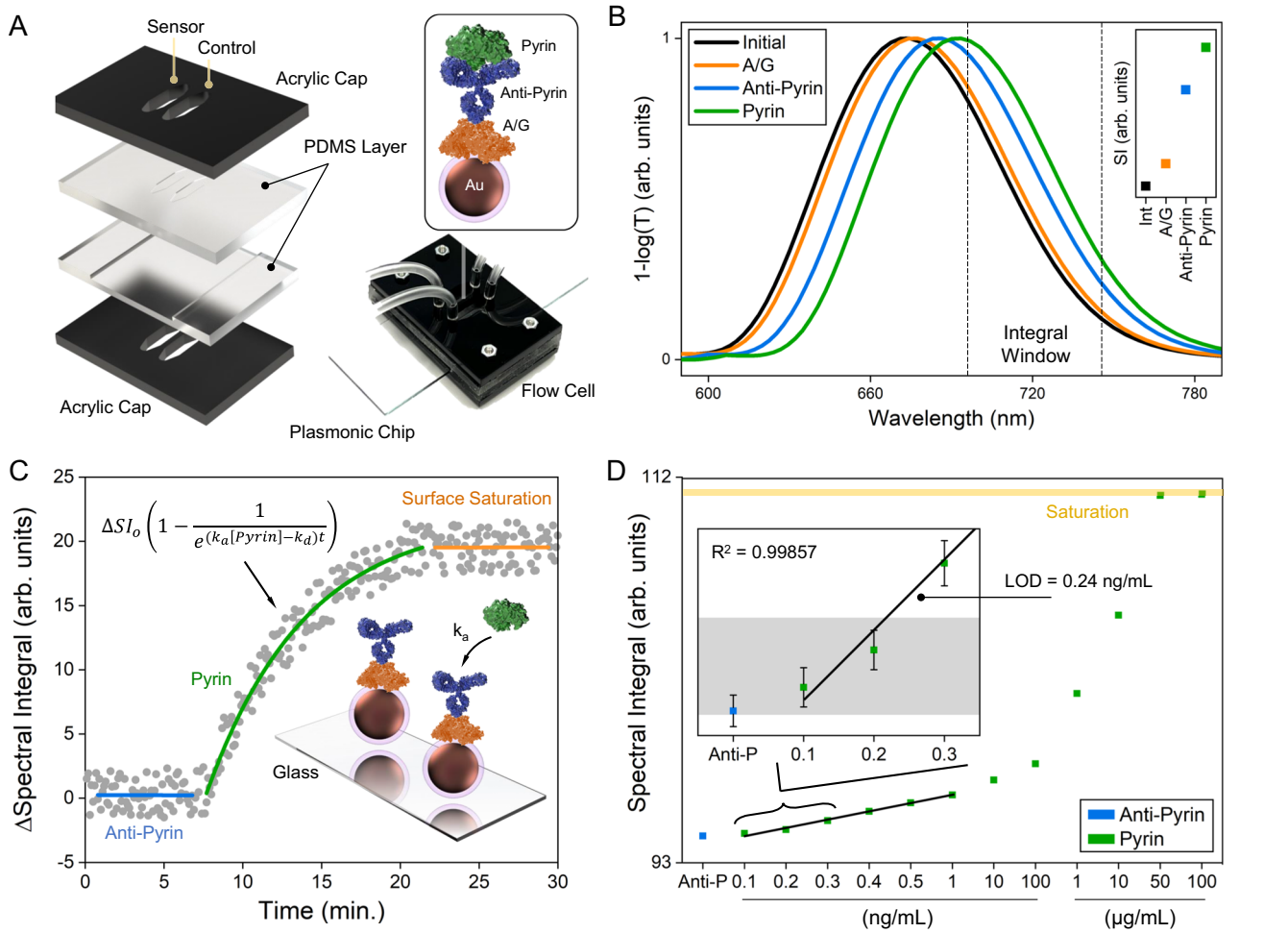


**Fig. 3 | Limit of detection of the pre-diagnostic platform. A** Schematic illustration and photograph of the PDMS-based flow cell holder, ensuring a leak-free flow cell. The figure inset demonstrates the surface modification technique used to capture the pyrin protein in the sensor channel of the flow cell. **B** Variation in the transmission resonance supported by the nanoparticles: initial response under PBS (black curve), after the addition of 100 μg/mL protein A/G (orange curve), 100 μg/mL anti-pyrin antibody (or IgG, blue curve), and 100 μg/mL pyrin protein (green curve) diluted with PBS solution (T = Optical transmission). The spectral window used for the spectral integral method is highlighted in gray. The figure inset presents the calculated spectral integral values for each transmission spectrum. **C** Real-time changes in the spectral integral value for the IgG-coated nanoparticles: initial response ($t$ = 0–6 min., blue curve), pyrin protein flowed over the sensing surface ($t$ = 6–21 min., green curve), and surface saturation with pyrin protein ($t$ = 21–30 min., orange curve). **D** Spectral integral values calculated for different pyrin concentrations (green squares) compared to protein IgG (blue square). The yellow line highlights the spectral integral values associated with the surface saturation case for pyrin protein. For each concentration, the spectral integral values were calculated after a 15-min pyrin injection. The figure inset zooms into a smaller pyrin concentration range. In the figure, squares correspond to the mean spectral values for $n$ = 10 independent experiments, and the error bars represent double the standard deviation. The black line corresponds to the linear regression model fitted to the calibration data to define the system LOD (limit of detection). Gray area highlights the overlapping spectral integral datasets for different conditions. The repetition tests were conducted for all pyrin concentrations, and the error bars are displayed only in the zoomed-in figure.

highly sensitive spectral information. By using a high concentration of pyrin protein, we demonstrated the maximum spectral shift achievable within the transmission resonance supported by the gold nanoparticles when their surface is fully covered with pyrin protein. Furthermore, as the biomass increases on the sensing surface, small variations in the amplitude of the transmission resonance can also be observed, which were eliminated by normalizing the spectral data.

Low pyrin concentrations in clinical samples can cause small spectral shifts within the plasmonic resonance, which can be challenging to track. Traditionally, spectral variations have been monitored at the wavelength of the plasmonic resonance (such as transmission or reflection maxima). However, this approach fails to provide sensitive sensing information in the presence of very low differences in refractive index[37]. The limit of detection capacity of label-free biosensing methods based on spectral tracking can be digitally improved using different data processing techniques. One potential approach is to simultaneously monitor spectral changes at multiple wavelengths instead of a single one[38]. This simultaneous monitoring could be achieved through their integration, accurately determining the presence of analytes at low concentrations. Here, the spectral integral method cumulatively evaluates spectral variations, where the transmission resonance is integrated within a spectral window, and the sum of all spectral changes within this region is used to determine the overall spectral change. Utilizing this method, we achieved a remarkable refractive index sensitivity of $2 \times 10^{-5}$ RIU (refractive index unit) through the employment of periodic gold nanohole arrays[38]. Moreover, this technique facilitates the monitoring of minute mass changes in cancer cells, with a mass accumulation rate on the order of picogram per hour[39]. Additionally, our method extends its applicability to nucleic acid sequencing via an integrated sensing-by-binding approach[40]. Considering that the transmission resonance shifted by ~18 nm after fully covering the sensing surface with protein A/G, anti-pyrin antibody, and pyrin protein, we positioned a 50 nm-wide spectral integral window at a wavelength that is 20 nm longer than the initial

position under PBS solution. The spectral window is highlighted in gray in Fig. 3B. We chose the position of the spectral integral window to be 2 nm longer than the transmission peak obtained when the surface was saturated with pyrin protein, which represents the longest wavelength position the plasmonic resonance could shift to. This choice eliminates the effects of the Lorentzian shape of the transmission resonance on the integral calculation, including only the right side of the transmission resonance in the spectral integral calculations[39]. As biomolecules attach to the sensing surface, the transmission resonance shifts toward longer wavelengths, overlapping well with the integral window. Consequently, larger transmission values fall within the integral window. As shown in Fig. 3B-inset, the spectral integral value increases as the biomolecular mass on the sensing surface increases.

It is essential to highlight that, for every test conducted with a plasmonic chip, the position of the spectral integral varies. This variation occurs because of the spectral position fluctuations inherent in our nanoparticle synthesis-based fabrication technique, as explained in the previous section. However, this methodology determining the position of the spectral integral window for each plasmonic chip, effectively eliminates the impact of these spectral variations when calculating the spectral integral values for different plasmonic chips.

As an additional note, the increase in the refractive index not only shifts the spectral position of the dipole but also broadens its linewidth. For example, the linewidth of the transmission resonance, ~51 nm, increases to ~76 nm after immersing the plasmonic chip in a PBS solution. However, for FMF diagnosis, we are comparing the transmission resonance obtained after the attachment of pyrin protein in the patient sample with that associated with anti-pyrin antibody, which does not cause a dramatic shift as in the case of the air-PBS interchange. For example, the total spectral shift from the antibody to 100 μg/mL pyrin protein results in only a ~1.6 nm linewidth broadening. Considering the much smaller spectral shifts in the presence of a smaller amount of pyrin protein in the patient samples, the broadening is expected to be much lower, resulting in a negligible impact on the spectral integral calculations.

Figure 3C shows the real-time spectral integral values calculated for nanoparticles coated with anti-pyrin antibody (100 μg/mL) as pyrin protein flows over the sensing surface. The stable integral value for anti-pyrin (blue curve) exhibits an exponential increase with the attachment of pyrin protein (100 μg/mL) to the nanoparticle surface (green curve). This exponential behavior is dependent on the association and disassociation constant ($k_a$, $k_d$) which governs the time-dependent molecular interaction between the anti-pyrin antibody and pyrin protein[41,42]. The time-dependent change in the spectral integral can be modeled as $\Delta SI(t) = \Delta SI_o\left(1 - e^{(-k_a[Pyrin] + k_d)t}\right)$, where [Pyrin] represents the concentration of pyrin protein and $\Delta SI_o$ is fit constant (See the Supplementary Information for the details of the derivation regarding this exponential relation[41]) After 15 min of pyrin injection, the sensing surface becomes saturated, resulting in a constant spectral integral value (orange curve).

Figure 3D illustrates the spectral integral values calculated at the end of a 15 min-long pyrin injection for different pyrin concentrations ranging from 0.1 ng/mL to 100 μg/mL (represented by green dots), along with the spectral integral value for 100 μg/mL anti-pyrin antibody (blue). We consistently observed an increase in the spectral integral value with higher pyrin concentrations. Once the concentration reaches 50 μg/mL, the sensing surface becomes fully saturated, resulting in no further variation in the spectral integral value for different concentrations (indicated by the yellow line). To determine the minimum detectable pyrin concentration using our pre-diagnostic biosensor, we conducted ten independent experiments for each concentration. The squares represent the mean integral values, and the error bars indicate double the standard deviation. In Fig. 3D-inset, we zoomed into the concentration range of 0.1 ng/mL–0.3 ng/mL. The spectral integral ranges obtained for anti-pyrin antibody (IgG), together with the 0.1 ng/mL and 0.2 ng/mL pyrin concentrations, showed an overlap and could not be reliably distinguished from each other. The overlaps between different conditions are highlighted with gray in the figure. However, we were able to differentiate the spectral integral value associated with the 0.3 ng/mL concentration from the others. To more precisely determine the limit of detection (LOD) for our pre-diagnostic biosensor, we applied a linear regression model to the spectral integral vs. IgG concentration data, which yielded an $R^2$ value of 0.99857. Using the formula LOD = $3.3\sigma/s$, where $\sigma$ represents the standard deviation of the signal and $s$ is the slope of the calibration curve, we determined the LOD to be 0.24 ng/mL[43]. Furthermore, using the relation LOQ = 10 σ/s, the limit of quantification of the system was calculated as 0.72 ng/mL[43]. Although the calibration curve exhibits linearity at lower concentrations, nonlinearity appears at higher concentrations likely due to surface saturation and mass transport limitations. However, for determining the LOD, linearity is required, so we focused on lower concentrations where the relationship remained linear, ensuring the fit was valid for LOD calculation. A sensitivity of 0.24 ng/mL (240 pg/mL) is not considered high, especially in comparison to SPR (Surface Plasmon Resonance)-based methodologies, which can achieve an LOD as sensitive as 10–100 pg/mL[44]. Metallic particle-enhanced periodic plasmonic structures have also been reported to achieve similar LODs[45]. Relative to these methodologies, our plasmonic chip supports a comparatively lower LOD, yet as shown in the following section, it is sufficient to distinguish between FMF+ and FMF− clinical samples based on the concentration of pyrin protein. Our clinical results confirm that our sensitivity level is adequate for this specific application. Besides, our fabrication method does not require expensive and sophisticated cleanroom facilities or complex and costly sample preparation, which is crucial for commercial applications. Furthermore, as demonstrated in the literature, there are several studies on metallic nanoparticle-based plasmonic chips that achieve higher LODs compared to ours[46]. In addition to our robust and sensitive hardware approach, our spectral post-processing methodology further improves the system's sensitivity, yielding better LODs compared to the classical nanoparticle-based plasmonic chips.

## Specificity of the biosensor platform

In addition to high sensitivity, it is crucial for a biosensor to possess high specificity to ensure accurate detection of target analytes in complex biological samples. Specificity minimizes false positives and enhances the reliability of the biosensor, making it an essential characteristic for accurate diagnostics and analytical applications[47]. To demonstrate specificity, we conducted both selectivity and interference tests. In our selectivity test, the plasmonic chips coated with anti-pyrin antibodies were exposed to pyrin protein together with some inflammatory proteins such as C-Reactive Protein (CRP), Tumor Necrosis Factor-alpha (TNF-α), Interleukin-6 (IL-6), and common proteins like Albumin, Immunoglobulin G (IgG), and Transferrin. Figure 4A-left shows the spectral integral values for the anti-pyrin antibody (100 μg/mL, blue bar), pyrin protein (10 ng/mL, green bar), and the other proteins (10 ng/mL, gray bars). In the figure, the bars represent the mean integral values of ten independent experiments, and the error bars indicate double the standard deviation. The change in the spectral integral upon the addition of pyrin protein was significant, while minimal changes were observed for the other proteins. To better demonstrate this behavior, we conducted Welch's $t$-test at a significance level of $\alpha = 5\%$, where α ranges between 0 and 1, and $p > 0.05$ indicates no significant difference. Using spectral integral values for each dataset, we compared the protein subsets with anti-pyrin, with $p$-values corrected using the Bonferroni method. Welch's $t$-test demonstrates an excellent separation from the antibody response for pyrin protein ($p = 3.74 \times 10^{-11}$), while inflammatory and serum proteins are indistinguishable from the antibody, e.g., $p > 0.13$ for all cases.

https://doi.org/10.1038/s41467-024-52961-8

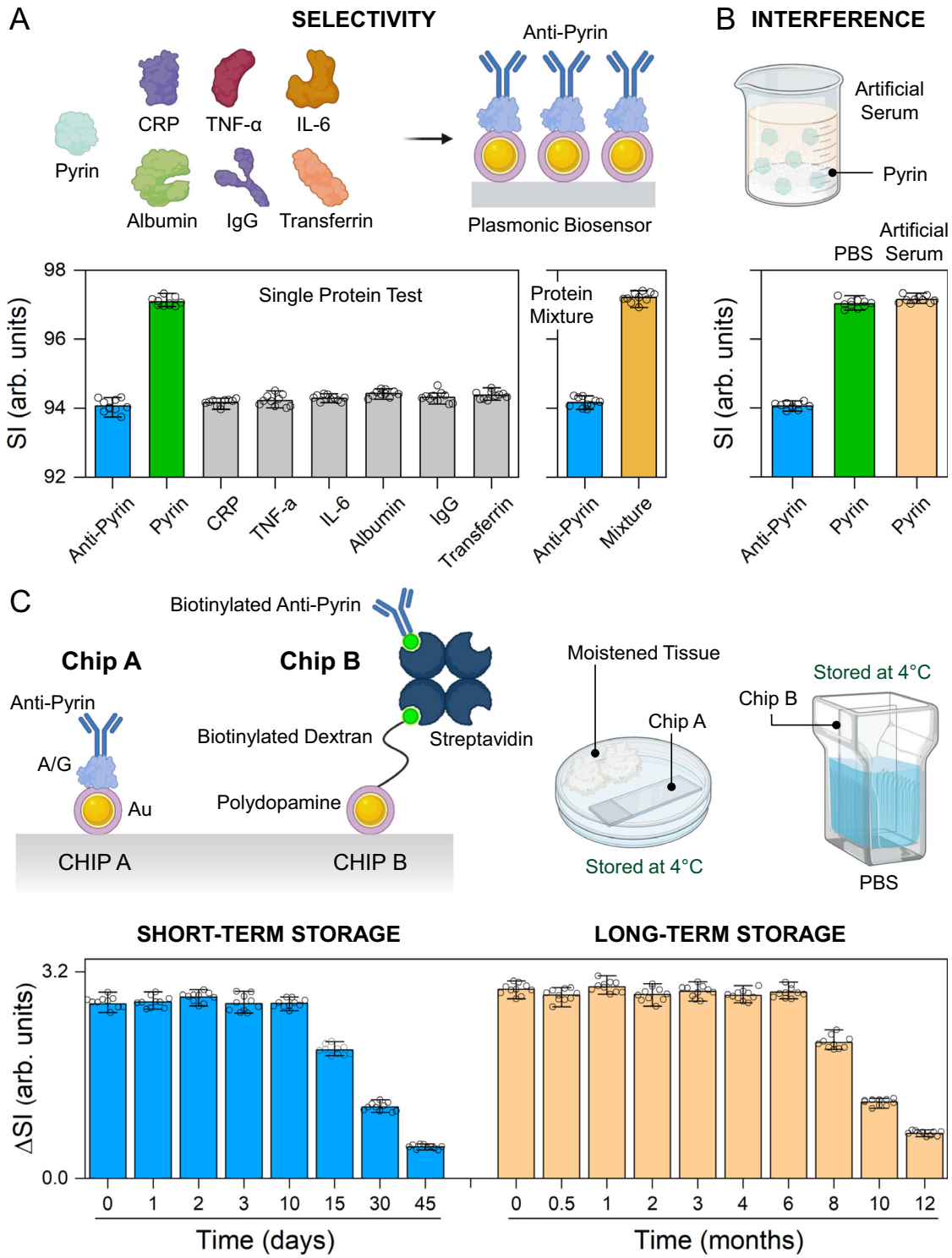


**Fig. 4 | Specificity and stability of the biosensor platform. A** Schematic illustration of the exposure of the plasmonic chip coated with anti-pyrin antibody to pyrin protein together with some common inflammatory and serum proteins for the selectivity test. (Left) Spectral integral values calculated for anti-pyrin antibody (blue bar), pyrin protein (green bar), and inflammatory and serum proteins (gray bars). Welch's *t*-test: *p* (anti-pyrin vs. pyrin) = $3.74 \times 10^{-11}$ and *p* (anti-pyrin vs. other proteins) > 0.13. (Right) Spectral integral values calculated for the anti-pyrin antibody (blue bar) and the protein mixture containing human pyrin CRP, TNF-α, IL-6, Albumin, IgG, and Transferrin proteins (yellow bar). Welch's *t*-test: *p* (single pyrin vs. protein mixture) = 0.21. **B** Spectral integral values calculated for the plasmonic chip coated with anti-pyrin antibody (blue bar) after the addition of pyrin protein under PBS (green bar) and artificial serum sample (peach bar). All measurements were conducted under PBS. Welch's *t*-test: p(PBS vs. Artificial Serum) = 0.19. **C** Schematic illustration of the two surface modification methodologies: Physisorption adapted for short-term storage and Streptavidin-biotin interaction adapted for long-term storage at 4 °C. Spectral integral values calculated for the plasmonic chips surface-modified via physisorption (blue bars) and streptavidin-biotin interaction (peach bars) for different storage durations. In the figures, bars correspond to the mean spectral integral values for $n = 10$ independent experiments, and the error bars represent double the standard deviation.

Furthermore, when exposed to a protein mixture (Fig. 4A-right) for the same concentrations, the plasmonic chip exhibited similar spectral integral values (yellow bar) to those obtained for single pyrin protein exposure (green bar). Similar behavior can be also seen from Welch's *t*-test, e.g., $p$ (single pyrin vs. protein mixture) = 0.21. This demonstrates that for the protein mixture, the spectral shifts were solely due to the attachment of pyrin protein on the sensing surface. In this section, our results highlight the exceptional selectivity of our biosensor platform, demonstrating its ability to accurately detect pyrin protein with minimal interference from other inflammatory and serum proteins.

For an ideal biosensor, minimizing interference is another critical parameter to ensure accurate detection of target analytes. To demonstrate this capability, we performed an interference test by adding pyrin protein to artificial serum that contains macromolecules, carrier proteins, hormones, growth factors, low molecular weight nutrients. As shown in Fig. 4B, immobilizing the 10 ng/mL pyrin protein on the sensing surface under PBS (green bar) and artificial serum (peach bar) exhibited similar spectral integral values, where p(PBS vs. Artificial Serum) = 0.19. This consistency underscores the high capability of our biosensor to eliminate interference from other serum components. These findings highlight the robustness and specificity of the biosensor, emphasizing its potential for reliable application in clinical diagnostics.

### Stability and shelf-life of ready-to-use plasmonic chips

Similar to technologies that rely on antibody-based sensing, our prediagnostic technology detects pyrin protein using its specific antibody. The performance of these antibodies depends significantly on storage conditions, as high temperatures can lead to degradation[48]. Like other examples, the anti-pyrin antibody and other ligands employed in our technology can be stored at 4 °C for short-term and at −20 °C for up to 6 months. For optimal analyte-ligand binding, freshly prepared antibody-coated surfaces could provide the highest sensitivity for biosensors[49]. Thanks to its system software, our technology allows operators to coat surfaces with various modification agents, enabling the use of fresh plasmonic chips for FMF analyses. While our point-of-care technology is designed for controlled environments like hospitals, the plasmonic chips could be prepared in ready-to-use format for high-throughput screening of FMF patients. Here, the ligand activity of our plasmonic chips can be preserved using methods similar to those in commercial SPR technologies, e.g., Bruker and Biacore™.

Figure 4C shows the spectral integral values for different storage durations, with bars representing the mean values from ten independent experiments and error bars indicating double the standard deviation. To store for up to two weeks, we added 500 μL of distilled water to the center of a petri dish and placed the plasmonic chips, which were prepared with physisorption for antibody attachment, on these water drops. A moistened lint-free tissue was placed into the dish to prevent evaporation during storage at 4 °C, and the dish was sealed with parafilm. This method successfully preserved the sensing capability of the plasmonic chips for ten days, as shown in Fig. 4C (blue bars).

When the coated surface needs to stay active for an extended period, maintaining moisture on the sensor surface is challenging. For functionalized plasmonic chips, this typically involves submerging them in a glass jar with 50 mL PBS. However, for plasmonic chips prepared via physisorption, this method may compromise binding stability due to the weak van der Waals forces used to attach antibodies. Submerging these chips can lead to antibody desorption, reducing their stability and sensing capability. Therefore, we opted for the streptavidin-biotin interaction, which provides a stronger and more stable attachment of antibodies (See the "Methods" section for the details of the surface modification methodology)[40]. In this strategy, the spin-coating step of streptavidin was conducted before inserting the plasmonic chip into the technology. In our plasmonic chips, polydopamine provides a versatile adhesive layer that can strongly attach to various substrates due to its ability to form strong covalent and non-covalent interactions. Dextran, a biocompatible polysaccharide, can be further modified with functional groups, e.g., biotinylation, to enable specific binding interactions. The combination of polydopamine and biotinylated dextran creates a stable and functional surface, providing strong binding and functional versatility. This method ensures that the biotinylated antibodies remain firmly attached to the streptavidin-coated chip surface, even during long-term storage in PBS, maintaining the chip's stability and sensing capabilities over extended periods. As shown in Fig. 4C (peach bars), the sensing capability of the plasmonic chips could be preserved for up to 6 months.

### Clinical sample tests

Figure 5A illustrates the schematic representation of the sample preparation process, as thoroughly described in the "Methods" Section. For each test conducted with FMF+ and FMF− clinical samples, the surface of the plasmonic chips was coated with 100 μg/mL protein A/G and 100 μg/mL anti-pyrin antibody. The total protein concentration varied for each sample, and they were subsequently diluted to a concentration of 0.1 μg/μL with PBS, as indicated in Table S1 and Table S2 in the Supplementary Information. This dilution strategy allowed for the reliable calculation of spectral integral values and the determination of their characteristic ranges for FMF+ and FMF− samples, independent of the total protein concentration. Moreover, since clinical samples contain a high number of other proteins that may interfere with the capturing of pyrin protein by its antibody, it was necessary to dilute the total protein concentration to an optimal value. This optimal value should be sufficiently high to create distinct spectral integral ranges for FMF+ and FMF− cases, while remaining low enough to minimize nonspecific bindings that could affect the binding between IgG and the pyrin protein (e.g., 0.1 μg/μL = 100 μg/mL). In the biodetection tests using clinical samples, the control and sensor channels were initially filled with PBS solution. The valve was then closed to prevent analyte binding in the control channel, while the sensor channel was sequentially coated with protein A/G and IgG. Subsequently, the valve was opened, and the clinical sample was flowed over both the control and sensor channels. Finally, PBS solution was infused to rinse both channels. The specificity of our technique is derived from the antibody's strong affinity to the pyrin protein, and the final washing step effectively removes unwanted proteins from the sensor surface.

Typically, control channels should be covered with antibodies that lack affinity for the targeted analytes. In our case, the determination of FMF status relies on quantifying the amount of pyrin protein in clinical samples. However, no other protein or biomarker specific to FMF has been identified to date[50–53]. The diagnosis of FMF is based on typical symptoms and nonspecific acute phase reactants such as C-reactive protein, fibrinogen, erythrocyte sedimentation rate, and serum amyloid A, all of which increase during an attack. Genetic tests confirm FMF by detecting variations in the genes encoding pyrin on chromosome 16. While serum amyloid A, fibrinogen, and C-reactive protein are acute phase proteins used to detect attacks in FMF patients, they are nonspecific inflammatory markers. In addition, proteins like resistin, calprotectin, pentraxin 3, CXC chemokine ligand 16, and serum soluble fasLigand are not specific to FMF. Their levels fluctuate during inflammation but lack diagnostic significance beyond indicating inflammation during an attack. Notably, their levels are normal during periods without attacks, rendering them unsuitable for assessing method specificity. Consequently, no other protein can serve as a control protein or antibody for control studies in our context.

Figure 5B displays the spectral integral values obtained from the control channel (gray bar) and the sensor channels (blue bar for healthy samples, red bar for FMF+ samples) in the analysis of clinical samples, consisting of 12 healthy and 18 patient samples. In each

https://doi.org/10.1038/s41467-024-52961-8

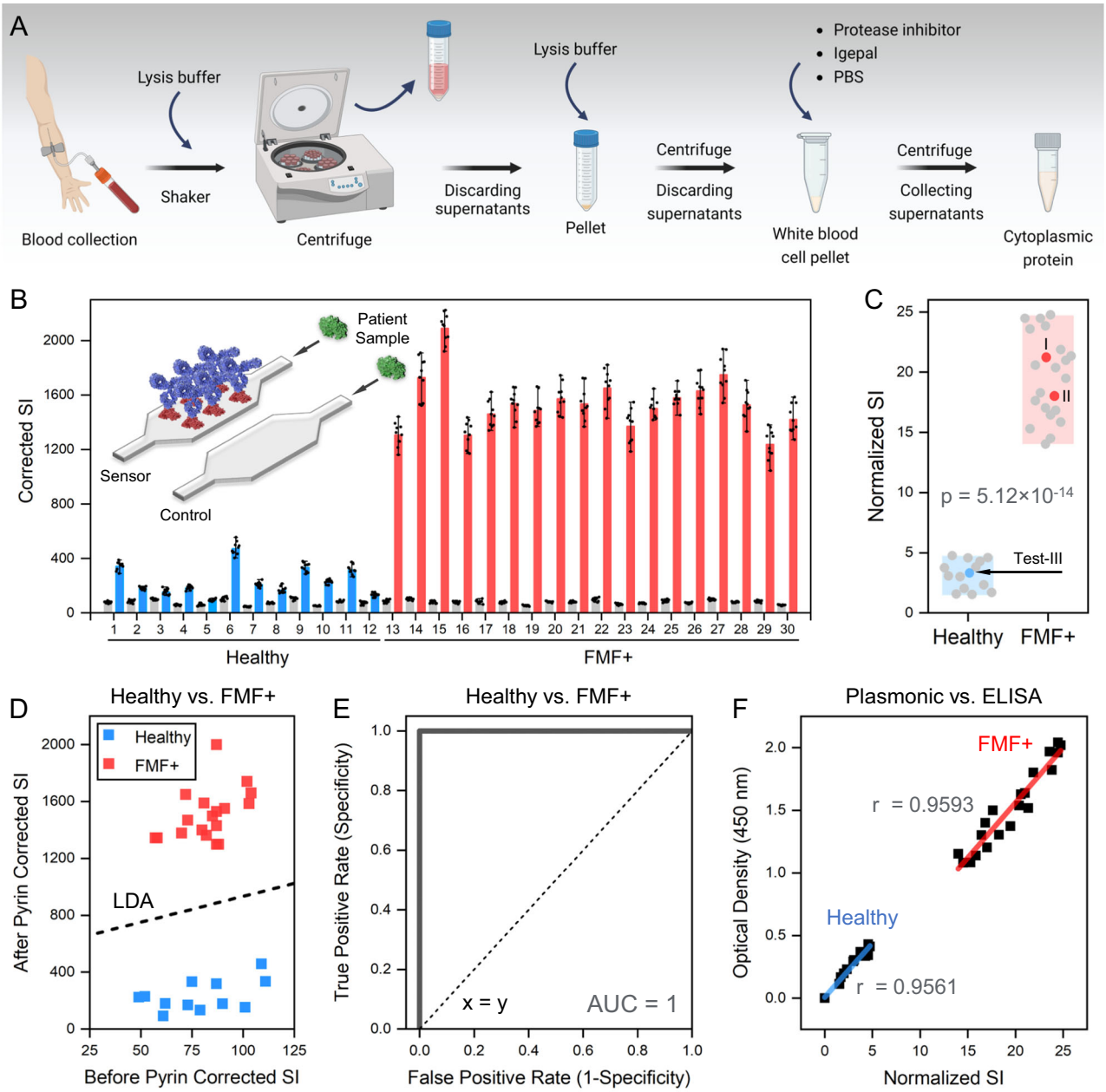


**Fig. 5 | Clinical tests with the pre-diagnostic platform. A** Schematic illustration depicting the collection and preparation of clinical samples. Created with BioRender.com. **B** Corrected spectral integral (SI) values determined for the control (gray bars) and sensor (blue bars: healthy samples, red bars: patient samples) channels in the flow cell. Total number of clinical samples, e.g., *n* (healthy) = 12 and *n* (patient) = 18. The figure inset shows the schematic illustration of the flow cell, where patient samples were flowed through the control (bare surface) and the sensor channels (surface coated with anti-pyrin antibody). In the figure, squares correspond to the mean spectral values for ten independent experiments, and the error bars represent double the standard deviation. **C** Normalized spectral integral values for healthy and patient samples. Blue and red boxes represent the spectral integral ranges for healthy and patient samples used in the system database. Inside the boxes, one blue dot (FMF−) and two red dots (FMF+) correspond to the clinical samples with successfully determined FMF status in single-blind tests. Welch's *t*-test: *p* (Healthy vs. FMF+) = $5.12 \times 10^{-14}$. **D** The two-dimensional spectral integral data determined before and after pyrin injection in the sensor region on the plasmonic chip, where an orthogonal LDA vector (black dashed line) separates the healthy (blue squares) and FMF+ subsets (red squares). **E** ROC analysis conducted between healthy and FMF+ samples, demonstrating and AUC of 1. As an additional note, both corrected and normalized spectral integral values were calculated via the division of two different spectral integral values, making them unitless parameters. **F** Comparison between normalized spectral integral values determined from the plasmonic pre-diagnostic technology and the optical density values determined from ELISA. In the figure, blue (healthy) and red lines (FMF+) account for the linear regressions fitted to the experimental data (black squares). Pearson's correlation coefficient: *r* (healthy) = 0.9561 (blue line) and r(FMF+) = 0.9593 (red line).

measurement, protein A/G, IgG, and clinical samples were flowed over the chip surface for 20 min, and subsequently, the spectral integral values for each analyte were calculated. Patient samples, diluted in PBS, were flowed over the plasmonic chip surface at a flow rate of 0.15 mL/min, which required a total of 3 mL of solution. For high reliability in determining spectral integral ranges corresponding to healthy and patient responses, spectral tests were repeated ten times. To ensure the accuracy of the control response, spectral integral values for the control channel were adjusted by dividing the spectral integral values determined after the final PBS wash (performed to remove unbound proteins from the surface) by the ones obtained after the initial PBS wash (representing the nanoparticle response under

PBS). This correction procedure validated that the control response exclusively accounted for nonspecific binding by eliminating the initial nanoparticle response and any external effects. For the sensor channel, the spectral integral values were corrected by dividing the spectral integral values obtained after the final PBS wash (representing the spectral integral value for the pyrin protein) by the ones determined for the anti-pyrin antibody. This correction step determines the spectral difference between the protein IgG and the pyrin protein, ensuring that the sensor response accurately represents the presence of the pyrin protein in the clinical samples. By dividing the integral values obtained for the sensor channel by those of the control region, we derived the normalized spectral integral values for each healthy and patient sample (Fig. 5C). This normalization process was necessary due to variations in the plasmonic resonances excited by the nanoparticles, which result from the particle synthesis method employed to fabricate the plasmonic chips. By following this methodology, we successfully eliminated the influence of nonspecific bindings and external factors such as optical and mechanical fluctuations on spectral integral calculations. Consequently, the obtained spectral information solely reflected the presence of the pyrin protein in the clinical samples. This approach not only facilitated the reduction in chip fabrication costs but also steered the development of a commercially viable product.

Figure 5B clearly illustrates the noticeable distinction between the spectral integral values obtained from healthy samples (blue bar) and patient samples (red bar). This distinction arises from the disparity in pyrin protein levels, while the relatively low spectral integral values calculated for control channels can be attributed to unspecific bindings. This differentiation, resulting from the higher pyrin protein levels in FMF+ samples compared to FMF−, is crucial for accurately determining the FMF status of the tested samples. In the figure, the squares represent the mean integral values of the data, and the error bars indicate a range of twice the standard deviation from these means, showing the variability in real values. Additionally, when considering the standard deviation as a percentage of the mean, a measure of relative variability, this relative standard deviation spans from 7% to 14% across the dataset. The consistency in the relative standard deviation across various measurements underscores the robustness of our hardware approach. This robustness was achieved by employing multiple spectrometers yielding high resolution, and the use of optical components that are spectrally compatible with each other, along with a casing designed to minimize optical, electrical, and mechanical fluctuations. Furthermore, our data processing methodology plays a crucial role in reducing errors due to fluctuations in the spectral measurement setup. This was accomplished by eliminating the spectral contribution of the background noise and the emission distribution of the light source, and simultaneously evaluating spectral features at different wavelengths, thereby enhancing the reliability and accuracy of our measurements. In Fig. 5C, the blue and red boxes represent the normalized spectral integral ranges for healthy and patient samples, respectively. These ranges were utilized to classify the tested clinical samples as either FMF− or FMF+. In the single-blind tests conducted with clinical samples, the normalized spectral integral values for two patient samples (red dots: Test-I and Test-II) and one healthy sample (blue dot: Test-III) fell within the defined spectral ranges. This outcome demonstrates that the spectral ranges employed in the system database successfully enable the determination of the FMF status of the clinical samples.

In order to demonstrate the robustness of the system's database in classifying healthy and FMF+ samples, we conducted Receiver Operating Characteristic (ROC) analysis following Linear Discriminant Analysis (LDA) for healthy (green bars) and FMF+ (red bars) in comparison to control datasets (gray bars). LDA projects the two-dimensional spectral integral data onto a single axis that optimally separates these two datasets and establishes a classification threshold. Fig. S12A in the Supplementary Information displays the two-dimensional data corresponding to the spectral integral values before (x-axis) and after (y-axis) the pyrin infusion in both the control and sensor regions on the plasmonic chip. In the figure, the dashed black lines represent the overlay of two orthogonal vectors, marking the threshold that separates the control group (gray squares) from the healthy (blue squares) and FMF+ data (red squares), demonstrating a greater distinction for the FMF+ group. Subsequently, we conducted ROC curve analysis and calculated the Area Under the Curve (AUC), a metric that assesses the accuracy of classifying each clinical sample as either healthy or FMF+[54]. To provide context, a random classifier would yield an AUC of 0.5, whereas a perfect classifier would have an AUC of 1. Figure S12B in the Supplementary Information shows the ROC curve conducted between the control and healthy group (blue curve) and between the control and FMF+ group (red curve). ROC analyses demonstrate an excellent resolution between the healthy and FMF+ datasets from the control group, with AUC values calculated as 0.9792 for the healthy group and 1 for the FMF+ group (Fig. SI2B-inset in the Supplementary Information). Using spectral integral values for each dataset, we compared the FMF− and FMF+ subsets with the control group, with $p$-values corrected using the Bonferroni method. Welch's t-test demonstrates excellent separation from the control group for both clinical datasets, with the FMF+ subset showing a higher distinction compared to the healthy samples, e.g., $p$ (Control vs. Healthy) = $5.68 \times 10^{-5}$ and $p$ (Control vs. FMF+) = $1.30 \times 10^{-27}$.

These statistical methods clearly demonstrate the perfect separation of clinical samples from the control group, ensuring the robustness of the system database. More importantly, classifying the clinical samples as healthy and FMF+ is critical to provide accurate test results. Using the normalized spectral integral data for healthy and FMF+ samples (Fig. 5C), Welch's $t$-test demonstrates their perfect separation, e.g., $p$ (Healthy vs. FMF+) = $5.12 \times 10^{-14}$. Figure 5D shows the two-dimensional spectral integral data for clinical samples, where the LDA vector (black dashed line) accurately distinguishes between healthy (green squares) and FMF+ datasets (red squares). ROC analysis (Fig. 5E) also demonstrates the perfect separation between healthy and FMF+ samples, yielding AUC = 1. These results confirm that the database created using the clinical samples, which exhibit distinctive spectral variations, is capable of accurately classifying the real samples as either healthy or patients.

## Validation of the plasmonic technology with a standard technique

In this study, we conducted a thorough evaluation of clinical samples using an innovative plasmonic pre-diagnostic technology. To validate our methodology, we compared our findings with those obtained through ELISA (enzyme-linked immunosorbent assay). ELISA is a sophisticated laboratory technique designed for the precise detection and quantification of proteins or antibodies within biological fluids[55]. Functioning on the principles of molecular recognition, ELISA operates akin to a lock-and-key system, where specific interactions occur between targeted molecules, namely antigens and antibodies. In the procedural sequence, the substances of interest are immobilized on a solid surface, thus initiating the assay. Stringent measures are then implemented to prevent nonspecific interactions. ELISA (LifeSpan BioSciences Inc.) used as a reference standard, possesses versatility in analyzing clinical samples like serum, blood, plasma, or supernatants. Its sensitivity of 0.094 ng/mL and a broad working concentration range from 0.156 to 10 ng/mL make it a reliable tool in clinical diagnostics. See the Supplementary Information for the details of the ELISA test and Fig. S13 for the standard calibration curve of the ELISA kit performed with pyrin protein. Figure 5F illustrates the results of our parallel analyses using both ELISA and our plasmonic biosensor on samples from both healthy individuals and those diagnosed with FMF. In the figure, the x-axis corresponds to the normalized spectral integral

https://doi.org/10.1038/s41467-024-52961-8

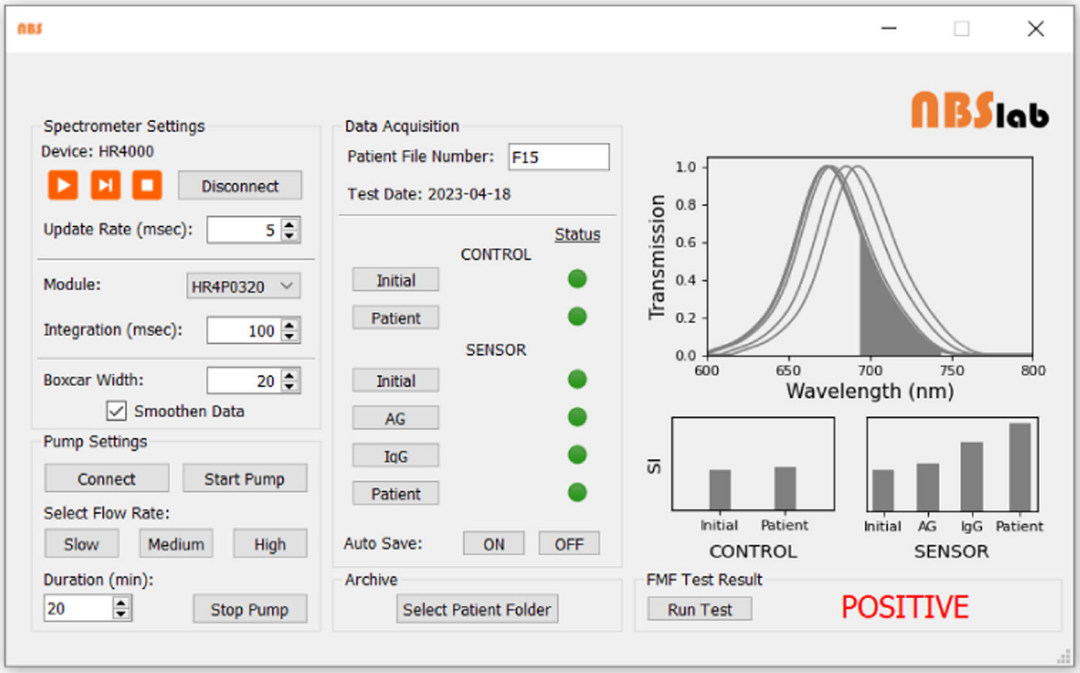


**Fig. 6 | Graphical User Interface (GUI) of the plasmonic pre-diagnostic platform.** The figure represents a particular case where a patient with file number F15 is being tested for Familial Mediterranean Fever. The spectrometer settings show the device name, with adjustable parameters such as update rate, integration time, and boxcar width to ensure smooth data collection. The selected flow rate is set to slow, and the pump duration (in minutes) is controlled to manage the delivery of fluids during testing. The data acquisition panel displays the test date, patient information, and control/sensor status. Transmission spectra show the signal at different wavelengths (600–800 nm), with the shaded area indicating the spectral integral window. The bar charts show the spectral integral (SI) values for control and sensor regions, comparing initial, AG, IgG, and patient samples. The FMF test result indicates a positive diagnosis, confirmed by the "POSITIVE" status in red.

values determined from our plasmonic methodology and the y-axis corresponds to the optical density values determined at 450 nm using a microplate reader in ELISA. Blue and red lines account for the linear regressions fitted to the experimental data (black squares) for the healthy and FMF+ clinical samples, respectively.

In order to quantitatively measure the agreement between our methodology with a clinical tool, we calculated Pearson's correlation coefficient, a robust statistical method to measure the linear correlation between two datasets. Our analysis revealed a high correlation between ELISA and our plasmonic biosensor as shown in Pearson's correlation coefficient ($r$) values, e.g., $r$ (healthy) = 0.9561 (blue line) and $r$ (FMF+) = 0.9593 (red line). In this context, Pearson's $r$ ranges from −1 to 1, signifying the strength and direction of a linear relationship. In our case, values near 1 indicate a nearly perfect positive linear relationship between the variables, emphasizing the precision and reliability of our plasmonic technology for clinical sample analyses. The significance of our findings extends beyond the high correlation, reaching into the realm of clinical relevance. The strength of the relationship, as indicated by Pearson's $r$ values exceeding the widely accepted threshold of 0.7 for a strong correlation[56], underscores the potential of our plasmonic biosensor as a robust and dependable clinical tool, comparable to the widely adopted ELISA method. Demonstrating a strong correlation with an FDA-approved technique (Food and Drug Administration) validates the clinical applicability of our plasmonic biosensor, paving the way for its integration into routine practice for FMF.

## System software

To control the system hardware from a single panel, we developed a graphical user interface (GUI) using Qt Designer and Python™ (Fig. 6). The GUI is responsible for determining the FMF status of clinical samples by calculating spectral integral values and identifying their ranges corresponding to either FMF+ or FMF−. It also provides access to the system hardware to execute surface modification steps by controlling analyte delivery with the piezo pump and acquiring data using spectrometers. The Spectrometer Settings panel allows the operator to connect to the spectrometers and configure parameters such as the data Update Rate (interval between each spectral signal generation), Integration time (duration for spectrometers to collect photons at each goniometer measurement point), and Boxcar Width. The Boxcar Width determines the number of pixels included in the average on each side of the center pixel for the manufacturer-defined boxcar averaging function used to smoothen the spectral data (Pixels Averaged = 2 × Boxcar width + 1). In the Pump Settings panel, the operator can connect to the piezo pump and choose from three different flow rates (Slow: 0.15 mL/min, Medium: 3 mL/min, and High: 6 mL/min) for a user-defined Duration (min).

The Data Acquisition panel enables the operator to perform spectral measurements for the control and sensor channels. These measurements include determining the initial chip response under PBS for both channels, the chip response after the attachment of protein A/G and IgG for the sensor channel, and the chip response after the attachment of clinical samples for both channels. The initial chip response is measured separately for the control and sensor channels to account for the spectral variations at different locations on the plasmonic chip caused by the random particle distribution resulting from the particle synthesis-based fabrication method. The position of the spectral integral window, highlighted with a gray area in the figure, is determined based on the initial transmission spectrum, and spectral integral values are calculated within this window. The transmission spectrum for each surface modification step is displayed on the panel, and the calculated spectral integral values are shown separately for the control and sensor channels. Each measurement involves determining transmission spectra (automatically normalized between 0 and 1)

https://doi.org/10.1038/s41467-024-52961-8

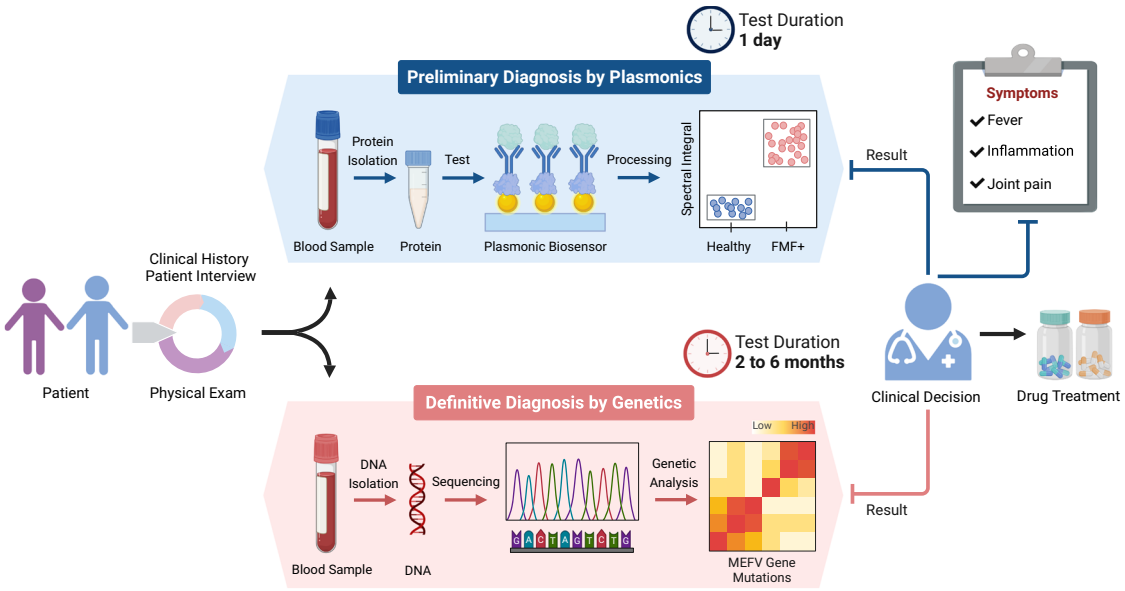


**Fig. 7 | Schematic illustration of preliminary diagnosis of FMF and initiating drug treatment based on clinical findings.** Initiating drug treatment in a timely manner through early diagnosis, while awaiting definitive diagnosis from genetic tests, can alleviate disease symptoms and greatly improve the quality of life. Created with BioRender.com.

20 min after the injection of targeted analytes using the piezo pump. The sequential operation of the pump, spectrometers, and spectral integral calculations for each step is automatically carried out through the GUI when the operator clicks on the associated icon on the Data Acquisition panel. Additionally, this panel allows the operator to archive all raw spectral data in a specific folder for each patient, including associated information such as Patient File Number and Test Date. In the Archive panel, the operator can retrieve all archived raw data for a clinical sample from a folder labeled with the patient file number. The FMF Test Result panel utilizes an algorithm to calculate the corrected and normalized spectral integral values for the clinical samples. It determines the range within which the calculated spectral integral value falls, providing the FMF status as either NEGATIVE or POSITIVE.

As an additional note, this section presents a detailed version of the GUI operated on a computer, showcasing the hardware settings panels to highlight the software's working principle. However, in practice, the hardware was operated through a Raspberry Pi directly integrated into the biosensor platform. The GUI for the Raspberry Pi was also developed using Qt Designer and Python™ (refer to Fig. S14 in Supplementary Information for images of the GUI). The compact version of the GUI includes all the settings found in the detailed version, with the distinction that the hardware settings were separated from the data acquisition and processing. In the Home panel of the compact version, the software automatically establishes connections with the spectrometers and pump. This allows the operator to focus solely on following the data acquisition steps for each surface modification. On the same panel, the operator can acquire and process spectral data in real-time or access archived data, perform the FMF test, and store the results. In the Hardware panel, the operator has the capability to modify the spectrometer settings for improved data quality and adjust pump settings for system cleaning purposes.

## Discussion

The most significant characteristic of the patient samples used to characterize and test our pre-diagnostic biosensor is that they were collected during routine doctor visits, rather than during acute attacks associated with FMF. During these attacks, individuals may experience symptoms of the disease such as abdominal and chest pains, joint complaints, and elevated levels of biomarkers like CRP (C-reactive protein), fibrinogen, and serum amyloid A. This constellation of symptoms is referred to as an acute phase response. Typically, the duration of these attack periods ranges from 1 to 3 days for most patients, and biomarker levels return to normal once the attacks subside. If a patient is not receiving treatment, these attacks may recur unpredictably. Of particular importance, the amount of pyrin protein in FMF patients is abnormally high during attack periods compared to non-attack periods (the intervals between attacks). Conversely, during non-attack periods, patients typically do not exhibit symptoms, and their laboratory test results are mostly within normal ranges. Therefore, the ability of our plasmonic biosensor technology to distinguish between FMF+ and FMF− individuals based on their pyrin levels, even during non-attack periods, is crucial for pre-diagnosing FMF during routine doctor visits. These findings highlight the high sensitivity of our plasmonic biosensor in discerning the pyrin protein levels between FMF+ and FMF− cases during non-attack periods, where the expected pyrin levels are generally lower than during attack periods.

The presented data suggests that our plasmonic biosensor holds the potential to serve as a pre-diagnostic tool for a rare disease. Our platform could aid physicians in initiating drug treatment for FMF patients by detecting abnormally synthesized pyrin protein in clinical samples. Figure 7 illustrates the overall procedure for FMF treatment, combining preliminary diagnosis and definitive diagnosis. Traditionally, during a routine doctor visit, the physician interviews the patient, conducts a physical examination, and investigates the clinical history, including the patient's record of FMF attacks and family history. Based on these clinical findings, the physician requests a genetic test to definitively diagnose the disease by detecting variants in the *MEFV* gene. However, receiving the genetic test results may take 2–6 months, which poses a considerable delay in initiating treatment for a disease with severe symptoms. To address this issue, an additional blood sample will be collected from the patient during the same doctor visit. A straightforward sample preparation protocol will be employed to extract cellular protein from the collected sample. The resulting protein solution will be tested using our plasmonic biosensor, which offers high selectivity and specificity in detecting the presence of pyrin protein. The biosensor technology will then determine the spectral

ranges associated with the protein levels in the clinical samples, thereby indicating the FMF status of the individual under investigation, whether FMF+ or FMF−. In the presence of symptoms and clinical findings suggestive of FMF, and based on the indicative results provided by our plasmonic biosensor, the physician will be able to initiate drug treatment. Finally, the genetic test results will be obtained to provide a definitive diagnosis of the disease, confirming the clinical case's status.

Based on recent studies, it is well-documented that the *MEFV* gene, responsible for encoding the pyrin protein on chromosome 16, harbors a total of 396 variants[57]. Notably, variants located within the exon 10 (B30.2) region have been established as having a higher pathogenic potential[58]. While pathogenic characteristics are evident in various exon and intron regions, in the realm of FMF, there exists a subset of variants categorized as "variants of unknown significance" (VUS) due to the uncertainty surrounding their clinical implications[59]. The clinical implications of these variations are not yet fully understood, leaving a gap in our comprehension of their impact on FMF. This uncertainty underscores the need for innovative solutions to better understand these genetic anomalies. Our technology emerges as a promising tool in this context, offering the potential to elucidate the pathogenicity of variants previously deemed uncertain and distinguishing individuals with heterozygous variants, particularly those displaying exon 10-enhanced features beyond the typical heterozygous pattern. In the future, by leveraging our technology, we could bridge the gap in knowledge regarding VUS, providing a clearer picture of their role in FMF and enhancing our ability to tailor more effective treatment strategies for affected individuals. Our findings emphasize the utility of our technique in differentiating between affected individuals, carriers, and those with VUS.

As an additional note, the main objective of this article was to develop a method for detecting patients during non-attack periods. The hypothesis is grounded in the observation that patients without attacks also exhibit elevated pyrin levels. Patients were enrolled after clinical and laboratory assessments confirmed the absence of FMF attacks. Blood samples were collected from these patients during non-attack periods, and individuals with inflammatory markers (such as C-reactive protein) within the normal range were included in the study. As a result, the levels of inflammatory markers (specifically C-reactive protein) measured were within the normal range. Furthermore, as previously mentioned, all patients involved in this study exhibited the M694V variant in the *MEFV* gene. It's important to note that the investigation into the connection between other *MEFV* variants and pyrin will be the focus of a forthcoming study, which has been planned based on the findings of this research.

In this study, the elevation of pyrin expression in the patient group is attributed to the influence of *MEFV* variants on pyrin synthesis, inflammatory attacks, and the impact of IL-1 levels. In literature, it has been shown that cytokines such as IFN-alpha and TNF, in particular, stimulate pyrin expression, although this has not been clearly elucidated[14,60]. On the other hand, there is no data regarding continuous stimulation of pyrin expression and a constant elevation in pyrin levels. There is no data available regarding the continuous high levels of pyrin in these patients. However, especially in disorders like FMF, the presence of pathogenic genetic mutations, exposure to a severe and continuous inflammatory process, and the stimulation of pyrin expression may lead to the detection of patients with high pyrin levels even during asymptomatic periods. Future research will delve into FMF and other inflammatory diseases, investigating the connections and distinctions between pyrin expression in relation to causes such as infection and trauma. This will necessitate testing our prediagnostic technology in a diverse range of individuals, including asymptomatic carriers, and patients with various *MEFV* variants, such as single heterozygous, complex heterozygous, and homozygous individuals. Additionally, the study will encompass a broader scope, exploring pyrin expression in the context of other rheumatic diseases, infections, and trauma.

In our future studies, we will also conduct a comprehensive evaluation of the sensitivity and specificity of our technology. These tests necessitate a diverse range of patient samples with different origins, which could potentially result in false negative or false positive outcomes, underscoring the importance of a large and varied patient sample pool. By utilizing clinical samples from individuals with asymptomatic carriers, featuring different *MEFV* variants, alongside cases of other rheumatic diseases and infections, we aim to establish a robust patient sample pool. This will allow us to assess potential false outcomes in the context of current clinical techniques, relying on both clinical observations and genetic tests. Through this process, we intend to challenge our technology to ascertain its limits and capabilities.

Our future research will also concentrate on differentiating FMF from infections and other inflammatory conditions that share similar symptoms with FMF. Our technology has proven effective in distinguishing individuals with FMF from healthy ones. However, when it comes to separating FMF from similar diseases, integrating clinical data could enhance the precision of our technology's results. The primary limitation in distinguishing these diseases lies in our technology's sensitivity, an area we aim to explore in greater depth through comprehensive future studies.

## Methods

The research presented in this article complies with all relevant ethical regulations. The authors obtained ethical approval to use patient and healthy samples from the Dokuz Eylul University Clinical Research Ethics Committee. In addition, informed written consent for the use of clinical samples was obtained from each volunteer donor.

### Statistics and reproducibility

No statistical method was used to predetermine the sample size. We collected data from a group consisting of 20 FMF patients and 13 control individuals, ranging in age from 0 to 18 years. Participants were recruited voluntarily. Participants' gender was not a parameter in this study. No data was collected based on participants' race, ethnicity, or other socially relevant groupings. No data was collected based on population characteristics. No data were excluded from the analyses. The investigators were single-blinded, e.g., the FMF status of the volunteers was known by the clinicians before delivering the clinical samples to the authors. The authors determined the FMF status of the samples using the presented technology and confirmed their results with the clinicians. The reproducibility of the experiments was confirmed via Welch's t-test at a significance level of $\alpha = 5\%$, and for all reproducibility tests, the $p$-values were greater than 0.05. Participants were randomly assigned. Data collection occurred during the patients' regular doctor visits. Volunteers in the control group scheduled their sample collection based on their availability. No specific instructions were given to the participants regarding their tests during the study.

### FDTD simulations

The simulations were performed using a unit cell that comprised a single particle, and perfectly matched layer boundary conditions were applied in all directions to model the behavior of the individual particle[61]. The refractive index values for gold and glass were obtained from reference[62]. A mesh size of 1 nm was selected for discretization along all directions. Consistent with the experimental configuration, we employed an unpolarized light source to illuminate the plasmonic structures.

### Surface modification for capturing pyrin protein

In the literature, various surface modification and chemistry methods have been proposed for capturing target analytes in detection

processes[63]. In our biosensor platform, the surface modification technique relies on the physical attachment of analytes to the sensing surface, specifically through physical adsorption or physisorption, which is facilitated by the presence of a polydopamine film on the gold nanoparticle surface. Microfluidics was employed for the targeted delivery of analytes to the sensing surface[34]. The process began by delivering 100 μg/mL protein A/G (Thermo Fisher Scientific Inc.) to the surface, which bonded to the active groups in the polymer structure. Protein A/G is a fusion protein that possesses binding sites for both protein A and protein G, exhibiting a high affinity for the Fc region of the anti-pyrin antibody (immunoglobulin G or IgG). Subsequently, antibody (Abcam Plc., ab154319) in 100 μg/mL concentration was introduced, and they attached to the A/G-coated sensing surface through their Fc region, forming a Y-shaped structure that exposes their binding sites (Fab regions) for pyrin protein[64]. In the final step, a commercially purified pyrin solution (Abcam Plc.) or a clinical sample containing pyrin proteins was infused, and the anti-pyrin antibodies captured these proteins on the sensing surface through their binding domains. In our surface modification method, after each immobilization step, the chip surface was rinsed with phosphate-buffered saline (PBS) to eliminate any unwanted proteins and biological agents from the surface.

For the selectivity test, human CRP, TNF-α, IL-6, Albumin, IgG, and Transferrin proteins were purchased from Sigma–Aldrich®. For the interference test, the artificial human serum was purchased from Sigma–Aldrich®. In both tests, to eliminate the effect of unbound proteins, the chip surface was thoroughly rinsed with PBS. This step ensures that any non-specifically bound proteins are removed, allowing us to accurately assess the sensor's response to the target pyrin protein.

For long-term storage of the functionalized plasmonic chips, we followed a streptavidin-biotin interaction-based surface modification methodology[40]. The chip surface was initially spin-coated with biotinylated dextran (Thermo Fisher Scientific Inc.). Following this, 25 nM streptavidin (Sigma–Aldrich®) was flowed over the sensing surface, ensuring a strong capturing mechanism to specifically target the biotinylated anti-pyrin antibody. Here, biotin is conjugated to the Fc region of the antibody leaving the antigen-binding sites free for target recognition. Finally, biotinylated anti-pyrin antibody (Picoband™) was immobilization on the sensing surface. This approach ensures stable and specific attachment, maintaining the chip's sensing capability over extended periods.

### Collecting healthy and patient samples

For the biosensing experiments, the clinical samples were tested in the form of serum. This approach was chosen because blood is a complex sample that contains a variety of biological materials, which could potentially lead to unspecific binding. The clinical and control group samples were obtained from Dokuz Eylul University, Department of Pediatric Rheumatology, Izmir, Turkey.

**Patient group.** The patient group consisted of 20 FMF patients, ranging in age from 0 to 18 years, who met the diagnostic criteria and were genetically diagnosed with FMF with exon 10 variants. All patients included in the study had at least one M694V variant. 14 of these are M694V homozygous, 6 are other exon 10 variants that form compound heterozygous variation with M694V. Table S3 in the Supplementary Information shows the *MEFV* Variations in the patient samples. The patients included in the study had complete file information, and their diagnosis was confirmed during follow-up visits. Out of the 20 patient samples, 18 were used for the system database, and 2 samples were used for system testing.

**Control group.** The control group consisted of 13 individuals, ranging in age from 0 to 18 years, who had not been clinically diagnosed with FMF and did not have a family history of FMF. Out of the 13 control samples, 12 were used for the system database, and 1 sample was used for system testing.

### Preparing healthy and patient samples

Pyrin is primarily expressed in neutrophils, eosinophils, monocytes, dendritic cells, and fibroblasts, and it plays a crucial role in regulating apoptosis, inflammation, and cytokine production. To isolate pyrin, cell lysates were prepared from whole blood samples obtained from patients. These whole blood samples were centrifuged with erythrocyte lysis buffer to separate leukocytes, which were subsequently homogenized using a vortex. The resulting leukocyte pellets were then mixed with a solution containing protease inhibitor, Octylphenyl Polyethylene Glycol, and PBS. Afterward, the tubes were centrifuged to collect the supernatants, which contained cytoplasmic proteins.

The protein isolation was carried out using the protocol described below[65]. Fig. 4A provides a schematic representation of the sample preparation protocol.

**White blood cell isolation.** Blood samples from each individual were collected in vacuum blood collection tubes containing 10 mL EDTA. To a sterile Falcon tube, 3 mL of red blood cell (RBC) lysis buffer was added for every 1 mL of blood sample, and the contents were mixed. The tubes were then centrifuged with a shaker at 625 × *g* for 15 min at room temperature to remove red blood cells, and the supernatants were discarded. To each pellet, 2 mL of RBC lysis buffer was added, and the pellets were re-suspended. The tubes were centrifuged again at 755 × *g* for 7 min. The supernatants were discarded, and the remaining white cells were homogenized using a vortex. This last step was repeated until completely RBC-free pellets were obtained.

**Protein isolation.** For the resulting white blood cell pellet, a 400 μL mixture consisting of 1× protease inhibitor (1%), Octylphenyl Polyethylene Glycol (Igepal, 1%), and PBS (98%) was prepared in a centrifuge tube. 200 μL of this mixture was added to each sample and mixed by pipetting to dissolve the cell pellet. The tubes were then centrifuged for 30 s, and the supernatants containing cytoplasmic proteins were collected. If necessary, the samples were stored at −80 °C for long-term storage.

### Reporting summary

Further information on research design is available in the Nature Portfolio Reporting Summary linked to this article.

## Data availability

Data supporting the findings of this study are available in the article, its Supplementary information, the source data file and from the corresponding author upon request. Source data are provided with this paper.

## Code availability

Code used to generate findings are available in Zenodo repository[66].

## References

1. Özen, S., Batu, E. D. & Demir, S. Familial Mediterranean Fever: recent developments in pathogenesis and new recommendations for management. *Front. Immunol.* **8**, 253 (2017).
2. Portincasa, P., Scaccianoce, G. & Palasciano, G. Familial Mediterranean fever: a fascinating model of inherited autoinflammatory disorder. *Eur. J. Clin. Invest.* **43**, 1314–1327 (2013).
3. Ben-Chetrit, E. & Touitou, I. Familial Mediterranean fever in the world. *Arthritis Rheum.* **61**, 1447–1453 (2009).
4. The French FMF Consortium. et al. A candidate gene for familial Mediterranean fever. *Nat. Genet.* **17**, 25–31 (1997).

5. Sood, R. et al. Construction of a 1-Mb restriction-mapped cosmid contig containing the candidate region for the familial Mediterranean fever locus (MEFV) on chromosome 16p13.3. *Genomics* **42**, 83–95 (1997).
6. Booty, M. G. et al. Familial Mediterranean fever with a single MEFV mutation: where is the second hit? *Arthritis Rheum.* **60**, 1851–1861 (2009).
7. Centola, M. The hereditary periodic fever syndromes: molecular analysis of a new family of inflammatory diseases. *Hum. Mol. Genet.* **7**, 1581–1588 (1998).
8. Livneh, A. et al. Criteria for the diagnosis of familial Mediterranean fever. *Arthritis Rheum.* **40**, 1879–1885 (1997).
9. Masters, S. L., Simon, A., Aksentijevich, I. & Kastner, D. L. Horror autoinflammaticus: the molecular pathophysiology of autoinflammatory disease. *Annu. Rev. Immunol.* **27**, 621–668 (2009).
10. Ozdogan, H. & Ugurlu, S. Familial Mediterranean fever. *Presse Med.* **48**, e61–e76 (2019).
11. Ozen, S. et al. EULAR recommendations for the management of familial Mediterranean fever. *Ann. Rheum. Dis.* **75**, 644–651 (2016).
12. Coker, I., Colak, A., Yolcu, I., Türkön, H. & Nalbantoglu, S. M. MEFV-Mutationsspektrum bei familiärem Mittelmeerfieber (FMF). *Z. Rheumatol.* **70**, 511–516 (2011).
13. Van Gijn, M. E. et al. New workflow for classification of genetic variants' pathogenicity applied to hereditary recurrent fevers by the International Study Group for Systemic Autoinflammatory Diseases (INSAID). *J. Med. Genet.* **55**, 530–537 (2018).
14. Heilig, R. & Broz, P. Function and mechanism of the pyrin inflammasome. *Eur. J. Immunol.* **48**, 230–238 (2018).
15. Bernot, A. Non-founder mutations in the MEFV gene establish this gene as the cause of familial Mediterranean fever (FMF). *Hum. Mol. Genet.* **7**, 1317–1325 (1998).
16. Mansfield, E. et al. The familial Mediterranean fever protein, pyrin, associates with microtubules and colocalizes with actin filaments. *Blood* **98**, 851–859 (2001).
17. Manukyan, G. & Aminov, R. Update on pyrin functions and mechanisms of familial Mediterranean fever. *Front. Microbiol.* **7**, 456 (2016).
18. Stella, A. et al. Familial Mediterranean fever: breaking all the (genetic) rules. *Rheumatology* **58**, 463–467 (2019).
19. Giancane, G. et al. Evidence-based recommendations for genetic diagnosis of familial Mediterranean fever. *Ann. Rheum. Dis.* **74**, 635–641 (2015).
20. Matzner, Y. et al. Expression of the familial Mediterranean fever gene and activity of the C5a inhibitor in human primary fibroblast cultures. *Blood* **96**, 727–731 (2000).
21. Yalçınkaya, F. et al. A new set of criteria for the diagnosis of familial Mediterranean fever in childhood. *Rheumatology* **48**, 395–398 (2009).
22. Shohat, M. & Halpern, G. J. Familial Mediterranean fever—A review. *Genet. Med.* **13**, 487–498 (2011).
23. Schmidt, J. et al. Genotyping of familial Mediterranean fever gene (MEFV)—Single nucleotide polymorphism—Comparison of Nanopore with conventional Sanger sequencing. *PLoS ONE* **17**, e0265622 (2022).
24. Zadeh, N., Getzug, T. & Grody, W. W. Diagnosis and management of familial Mediterranean fever: integrating medical genetics in a dedicated interdisciplinary clinic. *Genet. Med.* **13**, 263–269 (2011).
25. Seckin, T., Vural, S. & Köytepe, S. Preparation and structural properties of Fe3O4–polyimide hybrid nanocomposites. *Polym. Bull.* **64**, 115–126 (2010).
26. Chen, H., Zhao, L., Chen, D. & Hu, W. Stabilization of gold nanoparticles on glass surface with polydopamine thin film for reliable LSPR sensing. *J. Colloid Interface Sci.* **460**, 258–263 (2015).
27. Stewart, M. E. et al. Nanostructured plasmonic sensors. *Chem. Rev.* **108**, 494–521 (2008).
28. Rao, X. et al. A comparison study of functional groups (Amine vs. Thiol) for immobilizing AuNPs on zeolite surface. *Nanomaterials* **9**, 1034 (2019).
29. Lyu, Y. et al. The interaction of amines with gold nanoparticles. *Adv. Mater.* https://doi.org/10.1002/adma.202211624 (2023).
30. Olmos-Asar, J. A., Ludueña, M. & Mariscal, M. M. Monolayer protected gold nanoparticles: the effect of the headgroup–Au interaction. *Phys. Chem. Chem. Phys.* **16**, 15979 (2014).
31. Pensa, E. et al. The chemistry of the sulfur–gold interface: in search of a unified model. *Acc. Chem. Res.* **45**, 1183–1192 (2012).
32. Pensa, E., Azofra, L. M., Salvarezza, R. C. & Carro, P. Effect of ligands on the stability of gold nanoclusters. *J. Phys. Chem. Lett.* **13**, 6475–6480 (2022).
33. Stec, H. M., Williams, R. J., Jones, T. S. & Hatton, R. A. Ultrathin transparent Au electrodes for organic photovoltaics fabricated using a mixed mono-molecular nucleation layer. *Adv. Funct. Mater.* **21**, 1709–1716 (2011).
34. Yanik, A. A., Huang, M., Artar, A., Chang, T. Y. & Altug, H. Integrated nanoplasmonic-nanofluidic biosensors with targeted delivery of analytes. *Appl. Phys. Lett.* **96**, 021101 (2010).
35. Mortensen, S. B. et al. Pyrin inflammasome activation abrogates interleukin-1 receptor antagonist, suggesting a new mechanism underlying familial Mediterranean fever pathogenesis. *Arthritis Rheumatol.* **73**, 2116–2126 (2021).
36. Chae, J. J. et al. Gain-of-function pyrin mutations induce NLRP3 protein-independent interleukin-1β activation and severe autoinflammation in mice. *Immunity* **34**, 755–768 (2011).
37. Cetin, A. E. & Topkaya, S. N. Photonic crystal and plasmonic nanohole based label-free biodetection. *Biosens. Bioelectron.* **132**, 196–202 (2019).
38. Cetin, A. E. et al. Plasmonic nanohole arrays on a robust hybrid substrate for highly sensitive label-free biosensing. *ACS Photonics* **2**, 1167–1174 (2015).
39. Cetin, A. E., Topkaya, S. N., Yalcin-Ozuysal, O. & Khademhosseini, A. Refractive index sensing for measuring single cell growth. *ACS Nano.* https://doi.org/10.1021/acsnano.1c04031 (2021).
40. Cetin, A. E. et al. Plasmonic sensor could enable label-free DNA sequencing. *ACS Sensors* **3**, 561–568 (2018).
41. Saha, K., Bender, F. & Gizeli, E. Comparative study of IgG binding to proteins G and A: nonequilibrium kinetic and binding constant determination with the acoustic waveguide device. *Anal. Chem.* **75**, 835–842 (2003).
42. Bronner, V., Tabul, M. & Bravman, T. Rapid screening and selection of optimal antibody capturing agents using the ProteOn XPR36 protein interaction array system. *Bio-Rad Tech. Note* **5820**, (2006).
43. Armbruster, D. A. & Pry, T. Limit of blank, limit of detection and limit of quantitation. *Clin. Biochem. Rev.* **29 (Suppl. 1)**, S49–S52 (2008).
44. Nguyen, H., Park, J., Kang, S. & Kim, M. Surface plasmon resonance: a versatile technique for biosensor applications. *Sensors* **15**, 10481–10510 (2015).
45. Belushkin, A., Yesilkoy, F. & Altug, H. Nanoparticle-enhanced plasmonic biosensor for digital biomarker detection in a microarray. *ACS Nano* **12**, 4453–4461 (2018).
46. Mukherji, S. & Shukla, G. Nanoplasmonic biosensors: current perspectives. *Nanobiosensors Dis. Diagnosis* https://doi.org/10.2147/NDD.S64843 (2015).
47. Shrivastav, A. M., Cvelbar, U. & Abdulhalim, I. A comprehensive review on plasmonic-based biosensors used in viral diagnostics. *Commun. Biol.* **4**, 70 (2021).
48. Luan, J. et al. Environmental stability of plasmonic biosensors based on natural versus artificial antibody. *Anal. Chem.* **90**, 7880–7887 (2018).
49. Byrne, B., Stack, E., Gilmartin, N. & O'Kennedy, R. Antibody-based sensors: principles, problems and potential for detection of pathogens and associated toxins. *Sensors* **9**, 4407–4445 (2009).

50. Kılıçaslan, E. et al. Assessment of serum resistin and plasma calprotectin levels as biomarkers of inflammation in patients with familial Mediterranean fever disease. *Mediterr. J. Rheumatol.* **33**, 322 (2022).
51. Bulut, M. et al. Higher pentraxin-3 levels are associated with inflammation in familial Mediterranean fever. *J. Clin. Lab. Anal.* **30**, 978–981 (2016).
52. Çakan, M. et al. Serum amyloid A as a biomarker in differentiating attacks of familial Mediterranean fever from acute febrile infections. *Clin. Rheumatol.* **39**, 249–253 (2020).
53. Ceri, M. et al. Serum soluble fas ligand levels in familial Mediterranean fever. *Ren. Fail.* **35**, 835–837 (2013).
54. Pencina, M. J., D'Agostino, R. B., D'Agostino, R. B. & Vasan, R. S. Evaluating the added predictive ability of a new marker: from area under the ROC curve to reclassification and beyond. *Stat. Med.* **27**, 157–172 (2008).
55. Lequin, R. M. Enzyme Immunoassay (EIA)/Enzyme-Linked Immunosorbent Assay (ELISA). *Clin. Chem.* **51**, 2415–2418 (2005).
56. Ratner, B. The correlation coefficient: Its values range between +1/−1, or do they? *J. Target., Meas. Anal. Mark.* **17**, 139–142 (2009).
57. Guilaine BOURSIER. MEFV sequence variants. Available at: https://infevers.umai-montpellier.fr/web/search.php?n=1.
58. Chirita, D. et al. Mutations in the B30.2 and the central helical scaffold domains of pyrin differentially affect inflammasome activation. *Cell Death Dis.* **14**, 213 (2023).
59. Makay, B. & Gülez, N. Long-term follow-up of paediatric MEFV carriers. *Clin. Rheumatol.* **37**, 1683–1687 (2018).
60. Simon, A., Van Der Meer, J. W. M. & Drenth, J. P. H. Familial autoinflammatory syndromes. In *Kelley and Firestein's Textbook of Rheumatology* 10th edn 2, Vol. 1–2, (Elsevier Inc., 2016).
61. Sun, F. et al. Single-shot imaging of surface molecular ionization in nanosystems. *Nanophotonics* **10**, 2651–2660 (2021).
62. Johnstone, A. H. CRC handbook of chemistry and physics. *J. Chem. Technol. Biotechnol.* **50**, 294–295 (2007).
63. Soler, M. & Lechuga, L. M. Biochemistry strategies for label-free optical sensor biofunctionalization: advances towards real applicability. *Anal. Bioanal. Chem.* **414**, 5071–5085 (2022).
64. Cetin, A. E. et al. Handheld high-throughput plasmonic biosensor using computational on-chip imaging. *Light Sci. Appl.* **3**, e122 (2014).
65. Sevinc, N. Analysis of MEFV variations, expression and pyrin levels in familial Mediterranean fever disease. (Istanbul Technical University, 2016).
66. Data processing code for spectral data. https://doi.org/10.5281/zenodo.13731628.


## Acknowledgements

A.E.C. acknowledges the support of The Scientific and Technological Research Council of Türkiye (TÜBİTAK) through the 1005 – National New Ideas and New Products Research Funding Program (Project No. 119E649). This study was also supported in part by the EU Horizon 2020 ERA Chairs Project RareBoost (Project No. 952346).

## Author contributions

A.E.C. served as the principal investigator and provided supervision and funding for the project. I.K.A., S.N.T., C.A., and A.E.C. conceptualized the idea. M.B.A., S.D.Y., F.K., and A.E.C. constructed the optical, mechanical, and electrical read-out setup. F.K. and A.E.C. conducted the label-free biosensing experiments. F.K., E.U., and B.M. carried out the patient sample collection and preparation. I.K.A., S.K., B.A., I.Y., and T.S. performed the nanoparticle synthesis. F.K. designed and fabricated all microfluidic apparatus. M.B.A. designed the system software. All authors contributed to the preparation of the manuscript.

## Competing interests

I.K.A., S.N.T., C.A., E.U., B.M., S.K., B.A., I.Y., T.S., and A.E.C. have a pending patent application for the pre-diagnostic technology presented in this paper. The remaining authors declare no competing interests.

## Additional information

**Supplementary information** The online version contains supplementary material available at https://doi.org/10.1038/s41467-024-52961-8.

**Correspondence** and requests for materials should be addressed to Arif E. Cetin.

**Peer review information** *Nature Communications* thanks Abdurrahman Tufan, and the other, anonymous, reviewer(s) for their contribution to the peer review of this work. A peer review file is available.